https://dx.doi.org/10.1016/j.renene.2023.04.142

Renewable Energy

Critical sky temperatures for passive radiative cooling

--Manuscript Draft--

Manuscript Number:	RENE-D-22-06769R1
Article Type:	Research Paper
Keywords:	Radiative cooling; radiative heat transfer; Sky temperature; Beer-Lambert Law; Micro-fabrication
Corresponding Author:	Christopher Y.H. Chao, Ph.D. Hong Kong, HONG KONG
First Author:	Ross Y. M. Wong
Order of Authors:	Ross Y. M. Wong
	C. Y. Tso
	S. Y. Jeong
	S. C. Fu
	Christopher Y.H. Chao, Ph.D.
Abstract:	Passive radiative coolers can preserve the surface temperature below ambient by simultaneously reflecting incoming solar radiation and emitting thermal radiation to the sky. Cooling performance is affected by various environmental factors which determine the atmospheric transmittance. As such, field investigations lack convergence and completion. And energy balance consideration is a cogitation on overall heat transfer by the radiative cooler that ignores the uncertainties abundant in field study. In this work, we examine the cooling performance under different subtropical weather conditions in Hong Kong and approach the problem based onregression modeling as an alternative. At nighttime, the response variable of surface temperature reduction can be correlated with a single predictor variable of sky temperature difference, which is a lumped parameter of ambient temperature, relative humidity, and cloud fraction. At daytime, it should be parametrized with an additional variable regarding solar intensity. The higher the thermal emissivity, the larger is the temperature reduction at nighttime, especially obvious for large sky temperature difference . And heavy solar heat load is absorbed by the coolers at daytime even they feature reasonably high solar reflectivity. In this regard, further increment in solar reflectivity poses the top priority in improving daytime radiative cooling performance.
Suggested Reviewers:	Fuqiang Wang wangfuqiang@hitwh.edu.hk
	Carlos FM Coimbra ccoimbra@ucsd.edu

Critical sky temperatures for passive radiative cooling

Ross Y. M. Wong[1], C. Y. Tso[2], S. Y. Jeong[3], S. C. Fu[4], Christopher Y. H. Chao[4,5,*]

[1] Department of Mechanical and Aerospace Engineering, The Hong Kong University of Science and Technology, Clear Water Bay, Hong Kong, China.

[2] School of Energy and Environment, City University of Hong Kong, Kowloon Tong, Hong Kong, China.

[3] George W. Woodruff School of Mechanical Engineering, Georgia Institute of Technology, Atlanta, GA 30332, USA.

[4] Department of Building Environment and Energy Engineering, The Hong Kong Polytechnic University, Hung Hom, Hong Kong, China.

[5] Department of Mechanical Engineering, The Hong Kong Polytechnic University, Hung Hom, Hong Kong, China.

Corresponding author:

Christopher Y. H. Chao, PhD

Department of Building Environment and Energy Engineering, The Hong Kong Polytechnic University, Hung Hom, Hong Kong, China

Department of Mechanical Engineering, The Hong Kong Polytechnic University, Hung Hom, Hong Kong, China

Email address: christopher.chao@polyu.edu.hk

Tel: +852 2766-4673

Word Count: 5,922

Highlights

- The higher the thermal emissivity, the larger is the temperature reduction at nighttime, especially obvious for large sky temperature difference
- Heavy solar heat load is absorbed by the radiative coolers at daytime even they feature reasonably high solar reflectivity.
- Further increment in solar reflectivity poses the top priority in improving daytime radiative cooling performance.

Critical sky temperatures for passive radiative cooling

Ross Y. M. Wong[1], C. Y. Tso[2], S. Y. Jeong[3], S. C. Fu[4], Christopher Y. H. Chao[4, 5*]

[1]*Department of Mechanical and Aerospace Engineering, The Hong Kong University of Science and Technology, Clear Water Bay, Hong Kong, China.*

[2]*School of Energy and Environment, City University of Hong Kong, Kowloon Tong, Hong Kong, China.*

[3]*George W. Woodruff School of Mechanical Engineering, Georgia Institute of Technology, Atlanta, GA 30332, USA.*

[4]*Department of Building Environment and Energy Engineering, The Hong Kong Polytechnic University, Hung Hom, Hong Kong, China.*

[5]*Department of Mechanical Engineering, The Hong Kong Polytechnic University, Hung Hom, Hong Kong, China.*

Abstract

Passive radiative coolers can preserve the surface temperature below ambient by simultaneously reflecting incoming solar radiation and emitting thermal radiation to the sky. Apart from thermo-optical properties of the materials, radiative cooling performance is affected by various environmental factors which determine the atmospheric transmittance. As such, field investigations lack convergence and completion. And energy balance consideration, which aids in interpreting the field investigative results, is a deterministic cogitation on convective and radiative heat transfer by the radiative cooler that ignores the uncertainties abundant in field study. In this work, we examine the cooling performance of radiative cooling materials under different subtropical weather conditions in Hong Kong and approach the problem based on probabilistic regression modeling as an alternative. At nighttime, the response variable of surface temperature reduction can be correlated with a single predictor variable of sky temperature difference, which is a lumped parameter of ambient temperature, relative humidity, and cloud fraction. At daytime, it should be parametrized with an additional variable regarding solar intensity. The regression analysis reveals that, the higher the thermal emissivity, the larger is the temperature reduction at nighttime, especially obvious for large sky temperature difference . And heavy solar heat load is absorbed by the coolers at daytime even they feature reasonably high solar reflectivity. In this regard, further increment in solar reflectivity poses the top priority in improving daytime radiative cooling performance.

Keywords: *Radiative cooling, Radiative heat transfer, Sky temperature, Beer-Lambert Law, Micro-fabrication*

**Corresponding author*

Postal address: Department of Building Environment and Energy Engineering and Department of Mechanical Engineering, The Hong Kong Polytechnic University, Hung Hom, Hong Kong, China.

Email address: christopher.chao@polyu.edu.hk

Nomenclature

a_1, a_2, a_3, a_4	empirical constants of clear sky temperature models.
b_1, b_2, b_3, b_4, b_5	empirical constants of cloudy sky temperature models.
c (m/s)	speed of light, 3×10^8 m/s.
d (g/kg dry air)	moisture content.
f_c (%)	cloud fraction.
h_c (W/m^2-°C)	convective heat transfer coefficient.
h_p (J-s)	Planck constant, 6.63×10^{-34} J-s.
I (W/m^2-μm)	spectral intensity.
$I_{AM1.5g}$ (W/m^2-μm)	air mass 1.5 global solar spectrum.
I_{bb} (W/m^2-μm)	spectral blackbody intensity.
I_{sky} (W/m^2)	atmospheric thermal radiation.
I_{sun} (W/m^2)	solar radiation.
$I_{sun}^{(0)}$ (W/m^2)	solar radiation at $T_{sky}^{(0)}$.
I_{sun}^{*}	dimensionless solar radiation.
K (m^2)	extinction cross section of extinctive particles.
K_c (m^2)	extinction cross section of clouds.
K_j (m^2)	species extinction cross section.
K_v (m^2)	extinction cross section of vapors.
k_b (J/K)	Boltzmann constant, 1.38×10^{-23} J/K.
N (/m^3)	number density of extinctive particles.
N_c (/m^3)	number density of clouds.
N_j (/m^3)	species number density.
$N_j^{(0)}$ (/m^3)	species number density at $T_{sky}^{(0)}$.
N_v (/m^3)	number density of vapors.
p_{atm} (hPa)	standard atmospheric pressure, 1013.25 hPa.
p_w (hPa)	partial pressure of water vapor.
R^2	coefficient of determination.
s (m)	optical path length.
S (m)	optical path length designated at ground.
T (°C) / (K)	temperature.
T_{amb} (°C) / (K)	ambient temperature.
T_{dew} (°C)	dew point temperature.
T_{sky} (°C) / (K)	sky temperature.

1	$T_{sky}^{(0)}$ (℃) / (K)	reference sky temperature.
2	$T_{w,0}$ (℃)	surface temperature.
3	$\hat{\beta}_0$, $\hat{\beta}_1$, $\hat{\beta}_2$	empirical coefficients of regression equations.
4	γ_0, γ_1, γ_2	empirical coefficients of Beer-Lambert law.
5	γ_1^*, γ_2^*	dimensionless empirical coefficients of Beer-Lambert law.
6	ΔT_{sky} (℃)	sky temperature difference.
7	$\Delta T_{sky}^{(0)}$ (℃)	reference sky temperature difference.
8	ΔT_{sky}^*	dimensionless sky temperature difference.
9	$\Delta T_{w,0}$ (℃)	surface temperature reduction.
10	ε	spectral emissivity/absorptivity of radiative cooler.
11	ε_{sky}	sky emissivity.
12	$\varepsilon_{sky,c}$	sky emissivity specific to a clear sky.
13	ε_{sl}	spectrally averaged solar emissivity/absorptivity of radiative cooler.
14	ε_{th}	spectrally averaged thermal emissivity/absorptivity of radiative cooler.
15	λ (μm)	wavelength.
16	σ (W/m^2-K^4)	Stefan-Boltzmann constant, 5.67×10^{-8} W/m^2-K^4.
17	$\hat{\sigma}$ (℃)	standard deviation of $\Delta T_{w,0}$.
18	ϕ (%)	relative humidity.

1. Introduction

A sky-facing surface emitting longwave radiation through the atmospheric window lying within 8-13 μm of the electromagnetic spectrum can preserve its temperature below ambient under a clear nocturnal sky. This is a result of passive radiative cooling. Utilizing a photonic radiative cooler composed of 7 layers of alternating silicon dioxide (SiO_2) and hafnium dioxide (HfO_2) mid-infrared emitter stacked on a silver (Ag) solar mirror, Raman et al. (2014) demonstrated radiative cooling under direct sunlight, reporting a device temperature of 5 °C below ambient and a cooling power of 40 W/m^2 [1]. Shortly afterwards, ultra-low device temperature, remarkable cooling power, flexible materials selection and scalable manufacturing feasibility were discovered [1 – 7]. Novel engineering applications, especially in HVAC and energy systems in buildings, were also inspired by radiative cooling [8 – 13]. Radiative cooling is expected to save tremendous amounts of energy and serve as the driving force behind the evolution of efficient HVAC design and energy use in the built environment.

However, radiative cooling performance may vary geographically. Despite fascinating field investigative results reported from North America, some studies conducted elsewhere failed to achieve sub-ambient daytime radiative cooling [14, 15]. Bao et al. developed and tested nanoparticle based solar reflecting thermal radiators in Shanghai, where the temperature and humidity were above 24 °C and 50 % respectively, but the device remained 3 – 10 °C above ambient at daytime [14]. Tso et al. compared the performance of Raman's photonic radiative cooler in vacuum and non-vacuum enclosures under the subtropical climate in Hong Kong but were not successful in reproducing daytime radiative cooling [1, 15]. Jeong et al. tested the modified titanium oxide photonic radiative cooler and bio-inspired polymeric radiative cooler, only the ones under solar shades were accomplishing in sub-ambient daytime radiative cooling [7, 16, 17]. Han et al. assessed Raman's photonic radiative cooler and enhanced specular reflective film under tropical climate in Singapore and attributed large solar intensity and high humidity counteract radiative cooling effect [1, 18]. Radiative cooling performance relies heavily on the transparency of the atmospheric window. Longwave radiation emitted by the radiative cooler penetrates through a clear sky, which accompanies a highly transparent atmospheric window without significant scattering, attenuation, and absorption. However, atmospheric transparency is a dynamic property interacting with local meteorological conditions and becoming blurred under a humid and cloudy sky. Consequently, considerable upwelling radiation can be absorbed and re-emitted. Besides shortwave solar radiation, atmospheric thermal emissions impose a heavy heat load on the cooler and can raise the temperature above ambient. Huang et al. studied the impact of humidity, cloudiness, and aerosol concentration, and revealed the geographical variance in radiative cooling performance quantitatively, where the estimated potential in Stanford and Hong Kong are 61 W/m^2 and 25 W/m^2 respectively. [19]. Han et al. offered a different viewpoint and identified higher solar radiance in Singapore is the major cause of degraded radiative cooling performance besides atmospheric thermal radiation, where the predicted cooling power limit is 30 W/m^2 [20]. Li et al. presented the radiative cooling resource map for the contiguous United States, and showed

the southwestern has the highest potential of 70 W/m^2, whereas the southeastern has the lowest potential of 30 W/m^2 [21]. Zhu et al. and Chen et al. developed similar radiative cooling resource maps for China independently and identified the northwestern has the highest potential of 70 – 90 W/m^2, whereas the southeastern has the lowest potential of 10 – 40 W/m^2 [22, 23].

Contrary to mainstream theoretical based investigation on the variance in radiative cooling performance arising from climatic factors, we approach the problem by mean of probabilistic regression modelling on collected surface temperature measurement at different subtropical weather conditions in Hong Kong. And, contrary to deterministic energy balance consideration concerning overall heat flow by the radiative cooler, statistical modelling is advantageous in tolerancing the uncertainties arising from time varying and uncontrolled atmospheric conditions abundant in field investigation. This paper is organized as follow. In Section 2, it reviews the empirical models of sky temperature, a lumped parameter of meteorological variables of ambient temperature, relative humidity, and cloudiness, quantifying the downwelling atmospheric radiation, available in the literature. In Section 3, it outlines the procedures of materials preparation and fabrication of two radiative coolers, and the setup of outdoor field investigation for surface temperature measurement. In Section 4, it discusses the nocturnal and diurnal radiative cooling performances separately. With the scattered pairs measured at different weather conditions, statistical correlation between the response variable regarding surface temperature and the predictor variable regarding sky temperature are established. Finally, it prospects the applications of statistical models for building scale and city scale energy saving prediction.

2. Empirical models of sky temperature and sky emissivity

In sky temperature modelling, the atmosphere can be interpreted as a grey body of sky emissivity ε_{sky} at the ambient temperature T_{amb}. ε_{sky} is defined by the downwelling atmospheric radiation in accordance with Stefan-Boltzmann equation, i.e.

$$I_{atm} = \varepsilon_{sky} \sigma T_{amb}^4 , \tag{1}$$

where $\sigma = 5.67 \times 10^{-8}$ W/m^2-K^4 is the Stefan-Boltzmann constant. And sky temperature T_{sky}, distinct from T_{amb}, can be viewed as the equivalence of atmospheric thermal intensity in absolute temperature scale, i.e. $I_{atm} = \sigma T_{sky}^4$. The radiative heat flux is identical to the one given by eq. (1). Hence, ε_{sky} and T_{sky} are inter-connected by

$$T_{sky} = \varepsilon_{sky}^{\frac{1}{4}} T_{amb} . \tag{2}$$

As ε_{sky} ranges from 0 to 1, T_{sky} is always lower than T_{amb}, i.e., $T_{sky} \le T_{amb}$. ε_{sky} can be measured by a pyrometer experimentally, simulated by an atmospheric radiative heat transfer model numerically, and estimated by a sky emissivity model empirically. A pyrometer produces an output voltage by scanning in situ infrared radiance within 4.5 – 100 μm, but it requires careful calibration to eliminate background radiation from buildings

and vegetations. A radiative transfer model evaluates the atmospheric spectral emissivity within 0.2 – 100 μm line-by-line upon comprehensive specification of absorbing gases, aerosol, water vapor, cloud characteristics, vertical temperature, and humidity profiles, as well as various secondary atmospheric variables [24, 25]. In contrast, an empirical model is simpler to apply, correlating ε_{sky} with fundamental meteorological variables measurable by the observatory. Since the 1910s, plenty of sky temperature models, falling into two categories regarding clear and cloudy skies, have been suggested.

2.1 Clear sky temperature model

Under a clear sky, suspended water vapors serve as the primary source of I_{atm}. Clear sky emissivity $\varepsilon_{sky,c}$ can be parametrized with meteorological variables like T_{amb} (in °C), relative humidity ϕ (in %), partial pressure of water p_w (in hPa), dew point temperature T_{dew} (in °C), and moisture content d (in g/kg dry air). These variables are not mutually independent, but inter-connected by Magnus equations [26] in the form of

$$p_w = 6.11\left(\frac{\phi}{100}\right)\exp\left(\frac{17.63T_{amb}}{T_{amb}+243.04}\right), \tag{3}$$

$$T_{dew} = \frac{243.04\ln\left(\frac{p_w}{6.11}\right)}{17.63-\ln\left(\frac{p_w}{6.11}\right)}, \tag{4}$$

and

$$d = \frac{0.62\,p_w}{p_{atm}-p_w}, \tag{5}$$

where $p_{atm} = 1013.25$ hPa is the standard atmospheric pressure. Table 1 (a) tabulates the clear sky temperature models available in the literature. A few attempts [28, 29] parametrized $\varepsilon_{sky,c}$ with a single variable of T_{amb}, but the mainstream correlated $\varepsilon_{sky,c}$ with two principal variables of T_{amb} and ϕ. Brunt formulated one of the earliest two-variable models, expressing $\varepsilon_{sky,c}$ as

$$\varepsilon_{sky,c} = a_1 + a_2 p_w^{\frac{1}{2}}, \tag{6}$$

where $a_1 = 0.52$ and $a_2 = 0.065$ are the empirical constants [27]. Afterwards, various parametric forms were suggested [28 – 42] and published models were also recalibrated [43 – 50]. These reports revealed the difficulties in the development of a universal sky temperature model because the models were established based on localized and biased meteorological data drawn from one or several weather stations. Li et al. might have analyzed the most comprehensive meteorological and radiation data, collected from 7 stations of the Surface Radiation Budget Network in the United States, located at Goodwin Creek (Mississippi), Bondville (Illinois), Penn State University (Pennsylvania), Fort Peck (Montana), Sioux Falls (South Dakota), Boulder (Colorado) and Desert Rock (Nevada). The meteorological data, covering climatic diversity in the northern hemisphere, were used to recalibrate the Brunt

model. With the renewed empirical constants of $a_1 = 0.62$ and $a_2 = 0.056$, root-mean-square errors were reduced by 2.8 – 58.9 % [50].

2.2 Cloudy sky temperature model

Clouds are clusters of liquid phase water and solid phase ices, absorbing and emitting longwave radiation more vigorously than gaseous phase vapors. To cater for additional heat load imposed by clouds, $\varepsilon_{sky,c}$ ought to be corrected by a factor regarding cloud fraction f_c, ranging from 0 to 1, and gauged by the naked eye [51], solar radiation measurement [52] and satellite imaging [53]. Table 1 (b) tabulates the cloudy sky temperature models available in the literature. Initially, cloudy sky emissivity ε_{sky} was suggested by multiplying $\varepsilon_{sky,c}$ by a factor depending on f_c only [35, 54]. Later, it was reformed by adding a corrective term dependant on, but not limited to, f_c [43, 50, 52, 55, 56]. Recently, ε_{sky}, proposed by Li et al., takes the form of

$$\varepsilon_{sky} = \varepsilon_{sky,c}\left(1 - b_1 f_c^{b_2}\right) + b_3 f_c^{b_4} \phi^{b_5}, \tag{7}$$

where $b_1 = 0.78$, $b_2 = 1$, $b_3 = 0.38$, $b_4 = 0.95$ and $b_5 = 0.17$ are the empirical constants and $\varepsilon_{sky,c}$ is the recalibrated Brunt clear sky emissivity given by eq. (6). The model outperforms the former ones by 15 – 32 % [48]. For $f_c = 0$, it represents the clear sky condition, and ε_{sky}, given by eq. (7) is reduced to $\varepsilon_{sky,c}$. Hence, cloudy sky temperature model is applicable for all sky conditions.

3. Methodology

3.1 Materials preparation and characterization

The first device to be examined was the polymeric radiative cooler suggested by Zou et al. [3]. The fabrication commenced with the cleaning of quartz substrate in a piranha solution at 120 ℃ for 10 minutes. After rinsing in deionized water and spin-drying, a 200 nm Ag film was deposited on one face in high vacuum of 10^{-6} torr by E-beam evaporation. Last, a 100 μm polydimethylsiloxane layer was spin-coated on another face at 1,000 rpm for 1 minute and cured in the oven at 80 ℃ for 1.5 hours.

The second was the photonic radiative cooler, modified based on the one proposed by Raman et al. [1]. The composition of two constituent dielectric materials remained unchanged, but HfO_2 layers were replaced by silicon nitride (Si_3N_4) featuring not only high visible light and near infrared transparency, but also strong 8 – 13 μm emissivity. Hence, thermal emissive layers could be grown by plasma enhanced chemical vapor deposition, benefitting from higher processing pressure and deposition rate, as well as shorter processing time, relative to physical vapor deposition. The fabrication began with sequential cleaning of silicon wafer in a piranha solution at 120 ℃ for 10 minutes and hydrofluoric acid at room temperature for 1 minute. After rinsing and spin-drying, 200 nm Ag and 20 nm titanium films were deposited on the substrate by E-beam evaporation. Then, dielectric films were grown for designated thicknesses by chemical vapor deposition in the presence of 13.56 MHz radio

frequency induced plasma at 0.9 torr. Platen and showerhead temperatures were held at 300 ℃ and 250 ℃ respectively. For SiO_2 deposition, precursor gases of saline, nitrous oxide, and nitrogen were reacted at a radio frequency power of 30 W. For Si_3N_4 deposition, precursor gases of saline, ammonia, nitrous oxide, and nitrogen were reacted at a power of 20 W.

Mid-infrared and visible light spectral absorptivity/emissivity ε were characterized by Fourier-transform infrared spectrometry and UV-Vis NIR spectrometry respectively. For wavelengths λ within 2.5 – 25 μm, measured spectral ε of polymeric and photonic radiative coolers are shown in Figure 1 (a). Atmospheric spectral transmittance at Mauna Kea [57], as a representative clear sky condition, is overlaid on the same graph for reference. Polymeric cooler displays superior broadband mid-infrared ε, whereas photonic cooler features moderate ε. Spectrally averaged thermal emissivity ε_{th} is defined as

$$\varepsilon_{th} = \frac{\int_{2.5-25\mu m} I_{bb}(\lambda,T)\varepsilon(\lambda)d\lambda}{\int_{2.5-25\mu m} I_{bb}(\lambda,T)d\lambda}, \tag{8}$$

where $I_{bb} = 2h_p c^2 \Big/ \lambda^5 \left(e^{h_p c/\lambda k_b T} - 1\right)$ is the blackbody radiance, $c = 3\times10^8$ m/s is the speed of light, $h_p = 6.63\times10^{-34}$ J-s is the Planck constant, $k_b = 1.38\times10^{-23}$ J/K is the Boltzmann constant and T is the absolute temperature, and ε_{th} value 86 % and 61 % for polymeric cooler and photonic cooler respectively, at a convenient reference T of 300 K. For λ within 0.25 – 2.5 μm, measured spectral ε of polymeric and photonic radiative coolers, as well as air mass 1.5 global solar radiance $I_{AM1.5g}$, are shown in Figure 1 (b). Polymeric cooler exhibits excellent reflectivity in an entire visible light regime despite strong ultra-violet absorption. Photonic cooler demonstrates comparable reflectivity for λ longer than 750 nm, but it undergoes absorption through a few discrete bands elsewhere. Spectrally averaged solar absorptivity ε_{sl} is defined as

$$\varepsilon_{sl} = \frac{\int_{0.25-2.5\mu m} I_{AM1.5g}(\lambda)\varepsilon(\lambda)d\lambda}{\int_{0.25-2.5\mu m} I_{AM1.5g}(\lambda)d\lambda}, \tag{9}$$

and ε_{sl} value 3.3 % and 9.5 % for polymeric cooler and photonic cooler respectively.

3.2 Setup for outdoor field investigations

Outdoor field investigations were conducted on the rooftop of the campus of The Hong Kong University of Science and Technology. Figure 2 shows the schematic diagram and picture of experimental setup. With reference to ref. (3), each radiative cooler was positioned on an annular acrylic holder, placed in a glass Petri dish, and covered by a polyethylene film. The assembly was fixed to a tripod laid on an aerogel blanket. Table 2 summarizes all the testing configurations. For each type of radiative cooler, one was exposed to direct sunlight, and one was shadowed by an external solar shade made up of two pieces of erecting polished aluminum foil of 45 cm in height and 50 cm in width facing the southeast and the southwest. Exposed coolers experienced both direct and diffuse

solar radiation, whereas shaded coolers could access the diffuse component only. As a control reference, a naked silicon wafer in the same enclosure was also examined. Local T_{amb} and $T_{w,0}$ were measured by T-type thermocouples and recorded by a data logging system. The thermocouple measuring T_{amb} was placed in the vicinity of experimental setup far away from any heat sources and guarded from direct sunlight by a solar shade, and the ones measuring $T_{w,0}$ were adhered to the back of samples. They were sampled every 1 s and deployed for the calculation of hourly averaged values. T-type thermocouples, along with the data logging system, were calibrated in a diluted ethylene glycol bath, and the range of measurement error is within 0.2 ℃.

4. Results and discussion

Figure 3 (a) depicts the temporary profiles of measured T_{amb} at site, and $T_{w,0}$ of all examined devices on a dry and cloudless day. It also shows the recorded hourly T_{amb}, ϕ, f_c and solar intensity I_{sun} from neighboring weather stations operated by The Hong Kong Observatory. Reported ϕ and f_c were as low as 20 – 65 % and 0 – 25 %, respectively. With a minor deviation from the recorded values by weather station, measured T_{amb} varied between 21.3 ℃ and 31.8 ℃. At nighttime, polymeric radiative coolers achieved the deepest surface temperature reduction $\Delta T_{w,0}$ of -7.2 ℃ relative to the ambient, i.e., $\Delta T_{w,0} = T_{w,0} - T_{amb}$, whereas photonic radiative coolers and silicon wafer displayed lighter $\Delta T_{w,0}$ of -6.5 ℃ and -4.7 ℃, respectively. Thus, nocturnal radiative cooling performance ranks in the ascending order of ε_{th} and is not altered by the shade because involved radiative heat exchanges are diffuse in nature. At daytime, all the shaded devices realized sub-ambient radiative cooling, where $\Delta T_{w,0}$ of polymeric cooler and photonic cooler were -7.7 ℃ and -5.4 ℃, respectively. Under direct exposure to the peak I_{sun} of 861 W/m^2, unshaded devices settled at significantly higher $T_{w,0}$, in which $T_{w,0}$ of polymeric cooler remained slightly below the ambient by -0.9 ℃, whereas $T_{w,0}$ of photonic cooler heavily exceeded the ambient by 13.7 ℃. Last, $T_{w,0}$ of silicon wafer was the highest at 70.6 ℃. Hence, diurnal radiative cooling performance critically depends on both ε_{th} and ε_{sl} that can be boosted by the blockage of direct solar illumination. Figure 3 (b) depicts the correspondences on a humid and cloudy day, when the recorded ϕ and f_c were as high as 79 – 97 % and 88 – 100 % respectively, and the measured T_{amb} ranged from 20.4 ℃ to 25.7 ℃. At nighttime, all devices exhibited profoundly reduced $\Delta T_{w,0}$, where $\Delta T_{w,0}$ of polymeric coolers, photonic coolers, and silicon wafer were -0.8 ℃, -0.5 ℃ and -0.4 ℃, respectively. At daytime, they climbed up to -0.2 ℃ below the ambient, 1.6 ℃ and 6.8 ℃ above the ambient under a decayed I_{sun} of 200 W/m^2 at noon. Shaded and unshaded devices displayed roughly equal $T_{w,0}$ throughout the day because debilitated and scattered solar incidence dominated the skies. It can be summarized that, besides the intrinsic thermo-optical properties of materials, radiative cooling performance can be significantly affected by a batch of external meteorological factors. Hence, the investigation under the same setting was repeated for 70 times at nighttime and 35 times at daytime. Under the peak solar radiance, unshaded radiative coolers could not realize sub-ambient radiative cooling in most of the cases. Prior to these investigations, a preliminary study was conducted, comparing $T_{w,0}$ of the same

radiative cooler in different enclosures. Besides glass petri dish, naked styrofoam, aluminized mylar decorated styroform and radiative cooling materials blend coated styrofoam were tested. All measured $T_{w,0}$ remained higher than T_{amb}. This was coincident with pervious reports on subtropical and tropical radiative cooling performance [15 – 18]. And $T_{w,0}$ of the radiative cooler enclosed by a petri dish was the lowest. It is because thermal insulation is unfavorable of net heat dissipation by the radiative coolers at super-ambient $T_{w,0}$. Glass, albeit mid-infrared absorbing, does not obstruct thermal radiative transfer significantly because major radiation propagates through the covering polyetheylene film in the sky-facing direction. It is also solar transparent, which does not absorb heat heavily under solar incidence. Subjected to wind convection, enclosure temperature can be kept near the ambient, and heat exchange between the sample and the enclosure can be minimized. This sustains the choice of petri dish as the system enclosure during gathering field investigative results for statistical analysis.

4.1 Nocturnal radiative cooling performance

To establish the correlation between a radiative cooling performance indicator and a representative meteorological factor, a reasonable selection for the response variable can be $\Delta T_{w,0}$, but an appropriate choice for the predictor variable remains unconcordant. From an energy balance consideration, net radiative heat exchange by the radiative cooler results from outfluxing emission proportional to $T_{w,0}^4$ and inflowing absorption proportional to T_{sky}^4 in the absence of solar heating. They share a common pre-factor of ε_{th} due to the identity in emissivity and absorptivity. Thanks to the small differences among T_{amb}, T_{sky} and $T_{w,0}$, component radiative heat fluxes can be expressed as a first order Taylor expansion about T_{amb}. Then, net radiative heat exchange can be scaled with a single lumped meteorological variable of sky temperature difference ΔT_{sky} defined as $\Delta T_{sky} = T_{sky} - T_{amb}$. It can be estimated by eq. (7) and associated equations based on collected values of T_{amb}, ϕ and f_c from weather stations. The parameter can also serve as an appropriate predictor variable, and thus, measured $\Delta T_{w,0}$ can be correlated with estimated ΔT_{sky}. Figure 4 shows the scatterplots of response variable of $\Delta T_{w,0}$ against predictor variable of ΔT_{sky} upon time-averaging, as well as the linear regression lines for different radiative cooling materials at nighttime. Table 3 tabulates the numeric values of statistical parameters regarding the linear regression model. From a statistical perspective, each data-pair scatters about the best fitted line whose equation can be expressed as $\Delta T_{w,0} = \hat{\beta}_0 + \hat{\beta}_1 \Delta T_{sky}$, where $\hat{\beta}_0$ is the intercept coefficient and $\hat{\beta}_1$ is the slope coefficient. They can be estimated by the least squared error method. $\hat{\beta}_0$ is the predicted value of $\Delta T_{w,0}$ at a ΔT_{sky} of 0 °C, ranging from -1.4 °C to -0.9 °C, and $\hat{\beta}_1$ is the expected increment in $\Delta T_{w,0}$ associated with a unit increment in ΔT_{sky}, varying from 0.33 to 0.48. Prospective $\hat{\beta}_0$ should be 0 °C because ΔT_{sky} is the prioritized driving force of radiative cooling. The incongruity, appearing in a systematic right shift in scatterplots and regression lines, as well as an underestimated $\hat{\beta}_0$ thereby, can be attributed to speciously estimated ΔT_{sky} by Li's model [50]. Moreover, the pre-factor of ΔT_{sky}, resulting from counterbalanced deterministic convective and linearized radiative heat flows equals $1-1/\left(1+4\varepsilon_{th}\sigma T_{amb}^3/h_c\right)$, where h_c is the convective heat transfer coefficient, and

values 0.49 and 0.40 for polymeric coolers and photonic coolers respectively, after substituting T_{amb} = 27 ℃ and h_c = 5.5 W/m^2-℃. $\hat{\beta}_1$ and the pre-factor share the same increasing trend with ε_{th}. The supposed h_c of 5.5 W/m^2-℃ is much smaller than the value reported by Zou et al. [3], which can be attributed to the difference in wind environment during field investigation. Measured and regressed $\Delta T_{w,0}$ are distinct by an unbiased random error, where the amount of variability inherent in the regression model can be represented by the variance $\hat{\sigma}^2$ of $\Delta T_{w,0}$, and the proportion of variation in $\Delta T_{w,0}$ predictable from ΔT_{sky} can be interpreted by the coefficient of determination R^2. $\hat{\sigma}^2$ vary in a broad range, but the standard deviations $\hat{\sigma}$, after normalization by the expected values of $\hat{\beta}_0 + \hat{\beta}_1 \Delta T_{sky}$ are almost invariant. For instance, $\hat{\sigma}$ value -0.17, -0.18 and -0.18 for unshaded polymeric cooler, photonic cooler, and silicon wafer, respectively, at a ΔT_{sky} of -10 ℃. Hence, deterministic factors impact on expected radiative cooling performance, but do not alter $\hat{\sigma}$ of random deviation. For shaded radiative coolers, $\hat{\sigma}^2$ are 11 – 15 % less than the ones for their unshaded counterparts. Due to wind sheltering, convective heat flow can be obstructed by wind approaching from certain directions, in which convective fluctuation may be the major cause of random deviation in cooling performance. Therefore, probabilistic factors do not affect averaged cooling performance, but incur an incalculable move in $\hat{\sigma}^2$. Last, R^2 lies within 0.63 and 0.7 for all devices, which denotes a substantial correlation between $\Delta T_{w,0}$ and ΔT_{sky}, but it does not show an unambiguous dependence on materials properties.

4.2 Diurnal radiative cooling performance

Solar absorption imposes an additional heat load on the radiative cooler at daytime. Diurnal radiative cooling performance is investigated under the peak I_{sun}. Figure 5 shows the scatterplots of response variable of $\Delta T_{w,0}$ against predictor variable of ΔT_{sky} upon time-averaging, as well as the bivariate linear regression lines for different radiative cooling materials at daytime. Table 4 (a) tabulates the numeric values of statistical parameters regarding the bivariate regression model. Shaded radiative coolers substantially keep a linear relationship between $\Delta T_{w,0}$ and ΔT_{sky}. For the polymeric cooler, estimated $\hat{\beta}_0$ and $\hat{\beta}_1$ are 1.0 ℃ and 0.51, respectively. For the photonic cooler, the respective values are 3.9 ℃ and 0.48. In contrast, exposed devices do not show an increased $\Delta T_{w,0}$ with decreasing ΔT_{sky}, but $T_{w,0}$ rises with decreasing ΔT_{sky}, rapidly for small ΔT_{sky}, and plateauing for large ΔT_{sky}. $\hat{\beta}_0$ and $\hat{\beta}_1$ do not reveal any traceable trends and interpretative physical meanings. For shaded radiative coolers, both $\hat{\sigma}^2$ and R^2 lie within statistically valid ranges. $\hat{\sigma}$ span from 1.1 ℃ to 1.4 ℃, equivalent to the relative errors of 23 – 28 % at a ΔT_{sky} of -5 ℃, and R^2 range from 0.67 to 0.78, promising an unbreakable correlation between ΔT_{sky} and $\Delta T_{w,0}$. For unshaded devices, owing to tremendous departure between measured datasets and regressed equations, $\hat{\sigma}^2$ and associated random errors are magnified enormously, but R^2 are reduced dramatically, questioning the linear coupling between ΔT_{sky} and $\Delta T_{w,0}$.

Bivariate linear regression model is deficient in describing daytime radiative cooling performance of exposed

radiative cooling materials. As such, it is essential to revise the model by introducing an extra predictor variable regarding solar heat load. Obviously, ΔT_{sky} and I_{sun} are not mutually independent variables, but I_{sun} should be regarded as a single variable function of ΔT_{sky}. Hence, the revised regression model takes the modified form of $\Delta T_{w,0} = \hat{\beta}_0 + \hat{\beta}_1 \Delta T_{sky} + \hat{\beta}_2 I_{sun}\left(\Delta T_{sky}\right)$, where $\hat{\beta}_2$ is the slope coefficient of I_{sun}. The explicit form of $I_{sun}\left(\Delta T_{sky}\right)$ ought to be pre-determined otherwise. From the interpretation of Beer-Lambert law [58, 59], spectral radiative extinction dI traversing a thin layer of medium is proportional to local spectral intensity I, number density N, and extinction cross-section K of extinctive particles, as well as medium thickness ds, i.e. $dI(\lambda, s) = -K(\lambda) N(s) I(\lambda, s) ds$. Radiative attenuation can be attributed to scattering and absorption by the medium, and hence, K is the sum of scattering and absorption cross-sections. For the atmosphere composed of multi-component gases and suspended particulates, the contribution of K by each species is additive, i.e., $K(\lambda) N(s) = \sum_j K_j(\lambda) N_j(s)$, where N_j and K_j are the number density and extinction cross-section of each species, respectively. As a result, the integral form of Beer-Lambert law can be written as

$$I(\lambda, s) = I(\lambda, 0) e^{-\int_s \sum_j K_j(\lambda) N_j(s') ds'} . \tag{10}$$

Constituent gases, like nitrogen, oxygen, and argon occupy permanent fractions in the atmosphere, whereas suspended particulates, like aerosols, water vapors, and clouds are time and space varying in concentration. Aerosols, abundant in desert and urban areas are produced by natural processes and human activities. In contrast, water vapors and clouds are mostly affected by climatic factors. They are stratified in the troposphere, where the concentrations are determined by local hydrological cycle via evaporation, condensation, precipitation, and large-scale transport processes. The variability shows a bimodal distribution, with the maximum at the subtropics of both hemispheres. A water molecule has a triatomic structure, forming an isosceles triangle. The arrangement permits three fundamental vibration modes of symmetry, bending and anti-symmetry, responsible for multiple solar and near infrared absorption bands at 940 nm, 1.1 μm, 1.38 μm and 1.87 μm. Clouds are clustered water droplets and ice crystals, characterized by phase and size distribution. The radii of water droplets cover from 1 μm to 20 μm, whereas the characteristic lengths of ice crystals typically exceed 10 μm [60]. Because of large particle size relative to λ, solar scattering is dominated by Mie scattering, where the major radiative flux advances. For a spherical water droplet, scattering and absorption cross-sections are dependent on particle size and a complex refractive index via serial coefficients of scattered wave functions, but not strongly dependent on λ [61]. For a group of randomly oriented hexagonal ice crystals, extinction properties are determined by the shape and orientation of individual obstacles with respect to incident light [60]. Obviously, complicated absorption and scattering mechanisms, as well as comprehensive specification of N_j and K_j for each atmospheric constituent throughout the optical path, do not facilitate practical implementation of Beer-Lambert law. In many circumstances, including this study, it is essential to recognize these changes with respect to climatic parameters like T_{sky} rather than their absolute values. Because of a small variation in T_{sky}, the term of $\sum_j K_j N_j$ in Beer-Lambert equation at any T_{sky} can be expressed as a Taylor's expansion about a reference T_{sky} of $T_{sky}^{(0)}$, where

a convenient choice of $T_{sky}^{(0)}$ can be taken as the lowest possible T_{sky} corresponding to $\phi = 0$ and $f_c = 0$. Hence, the contributions from water vapors and clouds become the only terms dynamic with T_{sky}. Further neglecting spectral variations in extinction cross-sections of vapors K_v and clouds K_c yields the territorial I_{sun} written as

$$I_{sun}\left(\Delta T_{sky}\right) = I_{sun}^{(0)} e^{-\left(\Delta T_{sky} - \Delta T_{sky}^{(0)}\right)\int_S \left[K_v \partial N_v(s')/\partial T_{sky} + K_c \partial N_c(s')/\partial T_{sky}\right] ds'}, \quad (11)$$

where $I_{sun}^{(0)} = \int_\lambda I(\lambda, 0) e^{-\int_s \sum_j K_j(\lambda) N_j^{(0)}(s') ds'} d\lambda$ represents the solar intensity at $T_{sky}^{(0)}$, which can be as high as 1,140 W/m^2 at low-to-mid altitude areas [62], $N_j^{(0)}$ is the species number density at $T_{sky}^{(0)}$ and S is the optical path length destinated at the ground upon integration of eq. (10) over all solar λ. Admittedly, constant K_v assumption may not stand because water vapors are spectrally selective solar absorbers as explained above.

Figure 6 (a) surveys the local historical meteorological data pairs of the peak I_{sun} against ΔT_{sky}, collected by the weather stations in the period of 2015 – 2017. They show a strong non-linearity between ΔT_{sky} and I_{sun}. In logarithm-normal scale, I_{sun} converges to a maximal value at which ΔT_{sky} reaches the largest value and decreases at distinct rates, predominantly as ΔT_{sky} reduces, and thus, the dataset is bounded by a triangular sector. The observation coincides with the description by eq. (11), where the peak I_{sun} valuing $I_{sun}^{(0)}$ is well-defined at $T_{sky}^{(0)}$ and the exponential declining rate equaling the integral of $-\int_S \left(K_v \partial N_v/\partial T_{sky} + K_c \partial N_c/\partial T_{sky}\right) ds'$ carries at least two degrees of freedom of ϕ and f_c via $\partial N_v/\partial T_{sky}$ and $\partial N_c/\partial T_{sky}$. In a semi-empirical treatment, it is essential to estimate the integral in normalized scale. Without normalization, predicted $T_{sky}^{(0)}$ (in K) by Li's sky temperature model is proportional to T_{amb}, implying that the apparent scattering center spans a finite line segment, but not a definite point. Upon normalization as dimensionless sky temperature difference ΔT_{sky}^* and dimensionless solar intensity I_{sun}^*, where $\Delta T_{sky}^* = \left(\Delta T_{sky}^{(0)} - \Delta T_{sky}\right)/\Delta T_{sky}^{(0)}$ and $I_{sun}^* = I_{sun}/I_{sun}^{(0)}$, the operation translates the scattering core to a unified point at (0, 1) and the dataset to the first quadrant. Figure 6 (b) depicts I_{sun}^* against ΔT_{sky}^*, and shows that the slopes of the upper bound and lower bound feature two distinct characteristic rates. At large ΔT_{sky}^* limit, estimated slopes are -0.177 and -0.536 for the upper bound and low bound, respectively. At small ΔT_{sky}^* limit, they are 0.119 and -7.150 for the upper bound and lower bound, respectively. For any ΔT_{sky}^* away from these limits, they are supposed to be the linear interpolations of two limiting characteristic rates for simplicity. The argument leads to a continuous change with ΔT_{sky}^*, though the true transition takes place sharply at an intermediate critical ΔT_{sky}^*. Hence, the integral in eq. (11) regarding the change in $\sum_j K_j N_j$ with respect to T_{sky} can be based on the best estimation of exponential declining rate taken as the average of two bounding slopes for regression purposes. Its empirical form in dimensionless scale can be written as $\gamma_1^* + 2\gamma_2^* \Delta T_{sky}$, where $\gamma_1^* = -0.178$ and $\gamma_2^* = -1.669$ are the empirical constants. Strictly speaking, the equivalence in dimensional scale ought to be expressed in terms of $\Delta T_{sky}^{(0)}$, but, upon setting $\Delta T_{sky}^{(0)}$ as a constant estimated at the averaged T_{amb} of the dataset, it can be simplified as $\gamma_1 + 2\gamma_2 \Delta T_{sky}$, where $\gamma_1 = -0.105\ ^\circ\text{C}^{-1}$ and $\gamma_2 = -1.403 \times 10^{-3}\ ^\circ\text{C}^{-2}$ are the empirical constants. As a result, eq. (11) upon simplification and the multivariate

regression equation become

$$I_{sun}\left(\Delta T_{sky}\right) = I_{sun}^{(0)} e^{\gamma_0 + \gamma_1 \Delta T_{sky} + \gamma_2 \Delta T_{sky}^2} \tag{12}$$

and $\Delta T_{w,0} = \hat{\beta}_0 + \hat{\beta}_1 \Delta T_{sky} + \hat{\beta}_2 e^{\gamma_0 + \gamma_1 \Delta T_{sky} + \gamma_2 \Delta T_{sky}^2}$ respectively, where $\gamma_0 = -1.936$ is the empirical constant.

Figure 5 also depicts the multivariate regression lines, and Table 4 (b) tabulates the numeric values of statistical parameters regarding the multivariate regression model. Compared to bivariate regression model, it provides a better fit with scattered data pairs, features decreased $\hat{\sigma}^2$, as well as increased R^2, and improves overall interpretability of the statistical model. For shaded radiative coolers, $\hat{\sigma}$ range from 1.1 ℃ to 1.4 ℃ and R^2 range from 0.69 to 0.79. The refinement is the least notable because without the action of direct solar illumination, bivariate regression model with a single predictor variable of ΔT_{sky} has rationalized radiative cooling performance. For exposed radiative coolers and silicon wafer, the advancement is more significant, revealing the crucial role of solar heat load on cooling performance. Even the radiative coolers feature reasonably high solar reflectivity. $\hat{\sigma}$ is reduced by 5 % to 2.0 ℃ and R^2 is more than doubled valuing 0.11 for polymeric cooler. The small random uncertainty affirms the reliability of the regression model, whereas the feeble correlation stems from the interaction of radiative cooling and solar heating. Undoubtedly, ΔT_{sky} retains the cardinal role for daytime radiative cooling performance, which is not only the direct measure of net atmospheric radiative heat dissipation, but also the best estimation on solar incidence. Net cooling effect can be impassive to ΔT_{sky}, resulting from in step escalation of radiative cooling and solar heating with increasing ΔT_{sky}. In contrast, $\hat{\sigma}$ are 3.0 ℃ and 9.0 ℃ for photonic cooler and silicon wafer, respectively, and R^2 are 0.58 and 0.54 for photonic cooler and silicon wafer, respectively. The revised regression model reduces the random uncertainty but reinforces the correlation between ΔT_{sky} and $\Delta T_{w,0}$. Compared to the polymeric cooler, relative errors remain the same order of magnitude, but R^2 increases are approximately 5 times. The substantial correlation is a consequence of out of step vitalization of radiative cooling and solar heating. $T_{w,0}$ climbs up with ΔT_{sky} predominantly, which implies that solar heating is overwhelming. this can be attributed to detrimental radiative cooling materials properties of low ε_{th} and solar reflectivity. Conversely, radiative cooling can become forceful, $T_{w,0}$ can be declining with increasing ΔT_{sky}, and even drop below the ambient at sufficiently large ΔT_{sky}, providing reconcilable materials properties of ε_{th} and solar reflectivity higher than benchmarked polymeric cooler. Undeniably, ΔT_{sky} might not be the unique dependent parameter of I_{sun}. Aerosol concentration, visibility, and more, could also be the influential factors [58]. Furthermore, ΔT_{sky} and I_{sun} are accepted the key impactors on daytime radiative cooling performance. Secondary factors are not identified and omitted in the statistical models. It can be noted from the fact that R^2 values featured by the multi-variate daytime radiative cooling model remain smaller than the ones of nighttime model. As such, the present statistical model offers a simplified overview on daytime radiative cooling performance, more precise models with promoted predictability and reliability are demanding for development.

4.3 Applications for building scale and city scale energy saving prediction

For building scale energy saving prediction, it can be done by coupling the established statistical models with building energy simulation models. Building energy simulations can be categorized as white box model-based simulation [63, 64] and black box data-driven simulation [65, 66]. The former solving zonal conservation of mass, momentum and energy requires comprehensive specification on building envelope, zoning, building system parameters, as well as occupancy, scheduling and weather data, and the empirical models enable a simple and direct computation of $T_{w,0}$ and associated parameters under different weather conditions. The later capturing direct correlation between building performance indicators and operation data needs on-site measurement data over a certain period, and the collected data-pairs offer training datasets for machine learning and data mining.

Last, for city scale energy saving prediction, radiative cooling potential at a specific site, i.e. a city, as a figure merit, is defined as the annual average cooling power of ideal radiative cooler featuring unity emissivity for λ within 8 – 13 μm and zero absorptivity elsewhere, where the cooling power is the net radiative heat dissipative by the radiative cooler at T_{amb} [21, 67]. Cooling power can be estimated by ΔT_{sky}, therefore, radiative cooling potential can be noted from the frequency distribution of ΔT_{sky}. Figure 6 (c) surveys the frequency distribution of ΔT_{sky}, estimated by meteorological data collected by the weather stations in Hong Kong, from 2015 to 2017. Comparing annual frequency distribution for different years, it can be regarded as time invariant. For ΔT_{sky} within the interval of -1 ℃ and 0 ℃, the frequencies differ by the most, from 36 % in 2016 to 28 % in 2017. The occurrence drops with ΔT_{sky} monotonically until it vanishes at ΔT_{sky} of -20 ℃ approximately. Mean and median ΔT_{sky} of 3-year frequency distribution are as low as -2.5 ℃ and -1.1 ℃ respectively. These are typical ΔT_{sky} distribution in the subtropics, arising from prevailing humid and cloudy climate. Frequently small ΔT_{sky} hinders the radiative cooling potential. With specified ideal optical properties, estimated radiative cooling potential is 4.7 W/m^2 at a mean ΔT_{sky} of -2.5 ℃. With specified ideal optical properties and ΔT_{sky}, radiative cooling potential can be estimated for Hong Kong, which is 4.7 W/m^2. This value is on per area basis, and the accumulative territorial radiative cooling potential over a year can be evaluated then, which is 165,116 TJ. This figure offers an insight on the upper bound of replaceable energy by a sustainable source. It fosters the comparison with current building energy use for space cooling at the city scale and projects possible energy saving due to chilled water harvesting by radiative cooling [67 – 70] in Hong Kong. As defined in ref. (67), energy conversion efficiency is the ratio of converted enthalpy by the working fluid to the radiative cooling potential and was shown around 10 % for weighty fluid temperature reduction by a proof-of-concept experiment. In Hong Kong, annual electricity spent on space cooling in buildings was 48,622 TJ in 2020 [71]. Assuming 10 % for the efficiency of radiative fluid cooling system and 5 for the coefficient of performance of commercial chiller, 6.8 % of the cooling demand can be replaced by radiative cooling prospectively. This may save the electricity consumption by 3,302

TJ, equivalent to reduced carbon dioxide emission by 642,000 tons [72].

5. Summary and conclusion

This study identifies sky temperature difference as a critical environmental factor impacting radiative cooling performance. Sky temperature is a direct measure on downwelling atmospheric thermal radiation. In the literature, plenty of empirical sky temperature models have been suggested, connecting sky emissivity and sky temperature with fundamental meteorological variables of ambient temperature, relative humidity, and cloud fraction. Polymeric and photonic radiative coolers were fabricated, characterized, and examined for radiative cooling performance under different subtropical weather conditions in Hong Kong. Field investigative results are analyzed based on probabilistic regression modelling. Nocturnal and diurnal radiative cooling performances are considered separately. At nighttime, response variable of surface temperature reduction can be correlated with a single predictor variable of sky temperature difference, where the correlations accompany coefficients of determination ranging from 0.63 to 0.70. At daytime, it should be parametrized with an additional variable regarding solar intensity, where the correlations associate coefficients of determination up to 0.79. Statistically, median sky temperature difference is as low as -1.1 ℃, but corresponding solar intensity is as high as 1,130 W/m^2 in Hong Kong. Prevalently small sky temperature difference and high solar intensity are the major causes of degraded daytime radiative cooling performance under a subtropical climate. Hence, to accommodate the climate, the enhancements in sky window emissivity and solar reflectivity raise the equally important issues in radiative cooling materials development.

Acknowledgement

We acknowledge the technical support from Nano-system Fabrication Facilities in The Hong Kong University of Science and Technology.

The research is funded by The Hong Kong Research Grant Council via General Research Fund account 11200022.

Table 1. A summary of (a) clear sky temperature model; and (b) cloudy sky temperature model available in the literature. T_{amb} is the ambient temperature, T_{dew} is the dew point temperature, ϕ is the relative humidity, p_w is the vapor pressure, d is the moisture content, f_c is the cloud fraction, ε_{sky} is the sky emissivity, and $\varepsilon_{sky,c}$ is the clear sky emissivity.

(a)

Author(s)	*Index of reference*	*Independent variable(s)*	*Empirical expression*	*Empirical constant(s)*
Brunt (1932)	(27)	p_w (hPa)	$\varepsilon_{sky,c} = a_1 + a_2 p_w^{\frac{1}{2}}$	$a_1 = 0.52$, $a_2 = 0.065$
Swinbank (1963)	(28)	T_{amb} (K)	$\varepsilon_{sky,c} = a_1 T_{amb}^{a_2}$	$a_1 = 9.4\times10^{-6}$, $a_2 = 2$
Idso and Jackson (1969)	(29)	T_{amb} (K)	$\varepsilon_{sky,c} = 1 - a_1 \exp\left[a_2 \left(273.15 - T_{amb}\right)^{a_3}\right]$	$a_1 = 0.26$, $a_2 = -7.8\times10^{-4}$, $a_3 = 2$
Staley and Jurica (1972)	(30)	p_w (hPa)	$\varepsilon_{sky,c} = a_1 p_w^{a_2}$	$a_1 = 0.67$, $a_2 = 0.08$
Brutsaert (1975)	(31)	T_{amb} (K), p_w (hPa)	$\varepsilon_{sky,c} = a_1 \left(\frac{p_w}{T_{amb}}\right)^{a_2}$	$a_1 = 1.24$, $a_2 = 0.14$
Satterlund (1979)	(32)	T_{amb} (K), p_w (hPa)	$\varepsilon_{sky,c} = a_1 \left[1 - \exp\left(-p_w^{\frac{T_{amb}}{a_2}}\right)\right]$	$a_1 = 1.08$, $a_2 = 2016$
Idso (1981)	(33)	T_{amb} (K), p_w (hPa)	$\varepsilon_{sky,c} = a_1 + a_2 p_w \exp\left(\frac{a_3}{T_{amb}}\right)$	$a_1 = 0.7$, $a_2 = 6\times10^{-5}$, $a_3 = 1500$
Berdahl and Fromberg (1982)	(34)	T_{dew} (°C)	$\varepsilon_{sky,c} = a_1 + a_2 T_{dew}$	$a_1 = 0.73$, $a_2 = 0.006$
Berdahl and Martin (1984)	(35)	T_{dew} (°C)	$\varepsilon_{sky,c} = a_1 + a_2 \left(\frac{T_{dew}}{100}\right) + a_3 \left(\frac{T_{dew}}{100}\right)^2$	$a_1 = 0.71$, $a_2 = 0.56$, $a_3 = 0.73$

Prata (1996)	(36)	T_{amb} (K), p_w (hPa)	$\varepsilon_{sky,c} = 1 - \left(1 + a_1 \frac{p_w}{T_{amb}}\right) \exp\left(-\sqrt{a_2 + a_1 a_3 \frac{p_w}{T_{amb}}}\right)$	$a_1 = 1.2$, $a_2 = 3$, $a_3 = 46.5$
Dilley and O'brien (1998)	(37)	T_{amb} (K), p_w (hPa)	$\varepsilon_{sky,c} = \frac{a_1 + a_2 \left(\frac{T_{amb}}{273.15}\right)^6 + a_3 \sqrt{0.186 \frac{p_w}{T_{amb}}}}{\sigma T_{amb}^4}$	$a_1 = 59.38$, $a_2 = 113.7$, $a_3 = 96.96$
Niemela et al. (2001)	(38)	p_w (hPa)	$\varepsilon_{sky,c} = a_1 + a_2 (p_w - a_3)$, if $p_w \geq a_3$ $\varepsilon_{sky,c} = a_1 - a_2 (p_w - a_3)$, if $p_w < a_3$	$a_1 = 0.72$, $a_2 = 0.009$, $a_3 = 2$
Iziomon et al. (2003)	(39)	T_{amb} (K), p_w (hPa)	$\varepsilon_{sky,c} = 1 - a_1 \exp\left(-10 \frac{p_w}{T_{amb}}\right)$	$a_1 = 0.35$
Ruckstuhl et al. (2007)	(40)	d (g/kg)	$\varepsilon_{sky,c} = a_1 (a_3 d - a_4)^{a_2}$	$a_1 = 147.8$, $a_2 = 0.26$, $a_3 = 2.4$, $a_4 = 1.6$
Dai and Fang (2014)	(41)	p_w (hPa)	$\varepsilon_{sky,c} = \left(a_1 + a_2 p_w^{a_3}\right)\left(\frac{p_{atm}}{1013}\right)^{a_4}$	$a_1 = 0.48$, $a_2 = 0.17$, $a_3 = 0.22$, $a_4 = 0.45$
Carmona et al. (2014)	(42)	T_{amb} (K), ϕ (%)	$\varepsilon_{sky,c} = a_1 + a_2 T_{amb} + a_3 \phi$	$a_1 = 0.34$, $a_2 = 3.4 \times 10^{-3}$, $a_3 = 1.9 \times 10^{-3}$

(b)

Author(s)	*Index of reference*	*Empirical expression*	*Empirical constant(s)*
Maykut and Church (1973)	(54)	$\varepsilon_{sky} = \varepsilon_{sky,c}\left(1+b_1 f_c^{b_2}\right)$	$b_1 = 0.22$, $b_2 = 2.75$
Berdahl and Martin (1984)	(35)	$\varepsilon_{sky} = \varepsilon_{sky,c}\left(1+b_1 f_c + b_2 f_c^2 + b_3 f_c^3\right)$	$b_1 = 0.022$, $b_2 = 3.5\times10^{-3}$, $b_2 = 2.8\times10^{-4}$
Konzelmann et al. (1994)	(55)	$\varepsilon_{sky} = \varepsilon_{sky,c}\left(1- f_c^4\right)+b_1 f_c^4$	$b_1 = 0.95$
Crawford and Duchon (1999)	(52)	$\varepsilon_{sky} = \varepsilon_{sky,c}\left(1- f_c\right)+b_1 f_c$	$b_1 = 1$
Duarte et al. (2006)	(56)	$\varepsilon_{sky} = \varepsilon_{sky,c}\left(1+b_1 f_c^{b_2}\right)$ or $\varepsilon_{sky} = \varepsilon_{sky,c}\left(1- f_c^{b_3}\right)+b_4 f_c^{b_5}$	$b_1 = 0.24$, $b_2 = 0.58$, $b_3 = 0.67$, $b_4 = 0.99$, $b_5 = 0.67$
Carmona et al. (2014)	(42)	$\varepsilon_{sky} = \varepsilon_{sky,c} + b_1 f_c$	$b_1 = 0.21$
Li et al. (2017)	(50)	$\varepsilon_{sky} = \varepsilon_{sky,c}\left(1-b_1 f_c^{b_2}\right)+b_3 f_c^{b_4}\phi^{b_5}$	$b_1 = 0.78$, $b_2 = 1$, $b_3 = 0.38$, $b_4 = 0.95$, $b_5 = 0.17$

Table 2. A summary of testing configurations for outdoor field investigations. ε_{th} is the spectrally averaged thermal emissivity and ε_{s} is the spectrally averaged solar absorptivity.

Index	*Materials*	ε_{th}	ε_{s}	*External shading*
1	Polymeric radiative cooler	86 %	3.3 %	Yes
2	Polymeric radiative cooler	86 %	3.3 %	No
3	Photonic radiative cooler	61 %	9.5 %	Yes
4	Photonic radiative cooler	61 %	9.5 %	No
5	Silicon wafer	-	-	No

Table 3. A summary of numeric values of statistical parameters regarding the linear regression analysis on nocturnal passive radiative performance. ΔT_{sky} is the sky temperature difference, $\Delta T_{w,0}$ is the surface temperature reduction, $\hat{\beta}_0$ is the intercept coefficient of regression equation, $\hat{\beta}_1$ is the slope coefficient of regression equation, $\hat{\sigma}^2$ is the variance of $\Delta T_{w,0}$, and R^2 is the coefficient of determination.

Regression equation: $\Delta T_{w,0} = \hat{\beta}_0 + \hat{\beta}_1 \Delta T_{sky}$					
Predictor variable: ΔT_{sky}					
Response variable: $\Delta T_{w,0}$					
Number of sampled observations: $n = 70$					
Index	*Testing device*	$\hat{\beta}_0$	$\hat{\beta}_1$	$\hat{\sigma}^2$	R^2
1	Shaded polymeric radiative cooler	-1.414	0.475	0.923	0.698
2	Unshaded polymeric radiative cooler	-1.361	0.481	1.083	0.669
3	Shaded photonic radiative cooler	-1.130	0.432	0.910	0.660
4	Unshaded photonic radiative cooler	-1.224	0.425	1.021	0.627
5	Silicon wafer	-0.948	0.328	0.555	0.648

Table 4. A summary of numeric values of statistical parameters regarding the (a) bivariate and (b) multivariate regression analysis on diurnal passive radiative performance. ΔT_{sky} is the sky temperature difference, $\Delta T_{w,0}$ is the surface temperature reduction, $\hat{\beta}_0$ is the intercept coefficient of regression equation, $\hat{\beta}_1$ is the slope coefficient of solar intensity I_{sun} of regression equation, $\hat{\beta}_2$ is the slope coefficient of regression equation, $\hat{\sigma}^2$ is the variance of $\Delta T_{w,0}$, and R^2 is the coefficient of determination.

(a)

Regression equation: $\Delta T_{w,0} = \hat{\beta}_0 + \hat{\beta}_1 \Delta T_{sky}$					
Predictor variable: ΔT_{sky}					
Response variable: $\Delta T_{w,0}$					
Number of sampled observations: $n = 35$					
Index	*Testing device*	$\hat{\beta}_0$	$\hat{\beta}_1$	$\hat{\sigma}^2$	R^2
1	Shaded polymeric radiative cooler	0.984	0.505	1.277	0.776
2	Unshaded polymeric radiative cooler	2.675	0.113	4.341	0.049
3	Shaded photonic radiative cooler	3.912	0.480	1.965	0.670
4	Unshaded photonic radiative cooler	6.643	-0.674	13.688	0.366
5	Silicon wafer	18.586	-2.029	111.548	0.391

(b)

	Regression equation: $\Delta T_{w,0} = \hat{\beta}_0 + \hat{\beta}_1 \Delta T_{sky} + \hat{\beta}_2 e^{\gamma_0 + \gamma_1 \Delta T_{sky} + \gamma_2 \Delta T_{sky}^2}$					
	Predictor variable(s): ΔT_{sky} and $e^{\gamma_0 + \gamma_1 \Delta T_{sky} + \gamma_2 \Delta T_{sky}^2}$					
	Response variable: $\Delta T_{w,0}$					
	Number of sampled observations: $n = 35$					
Index	*Testing device*	$\hat{\beta}_0$	$\hat{\beta}_1$	$\hat{\beta}_2$	$\hat{\sigma}^2$	R^2
1	Shaded polymeric radiative cooler	-1.701	1.051	21.987	1.254	0.787
2	Unshaded polymeric radiative cooler	10.438	-1.467	-63.577	3.95	0.108
3	Shaded photonic radiative cooler	7.098	-0.169	-26.093	1.938	0.685
4	Unshaded photonic radiative cooler	31.226	-5.676	-201.310	8.775	0.578
5	Silicon wafer	80.873	-14.704	-510.076	81.15	0.543

Figure 1. (a) Spectral emissivity/absorptivity $\varepsilon(\lambda)$ of polymeric and photonic radiative coolers within 2.5 - 25 μm characterized by Fourier transform infrared spectrometry and referring to atmospheric radiative spectrum at Mauna Kea [57]. (b) Spectral emissivity/absorptivity $\varepsilon(\lambda)$ of polymeric and photonic radiative coolers within 250 nm - 2.5 μm characterized by UV-Vis NIR spectrometry and referring to air mass 1.5 global solar spectrum.

(a)

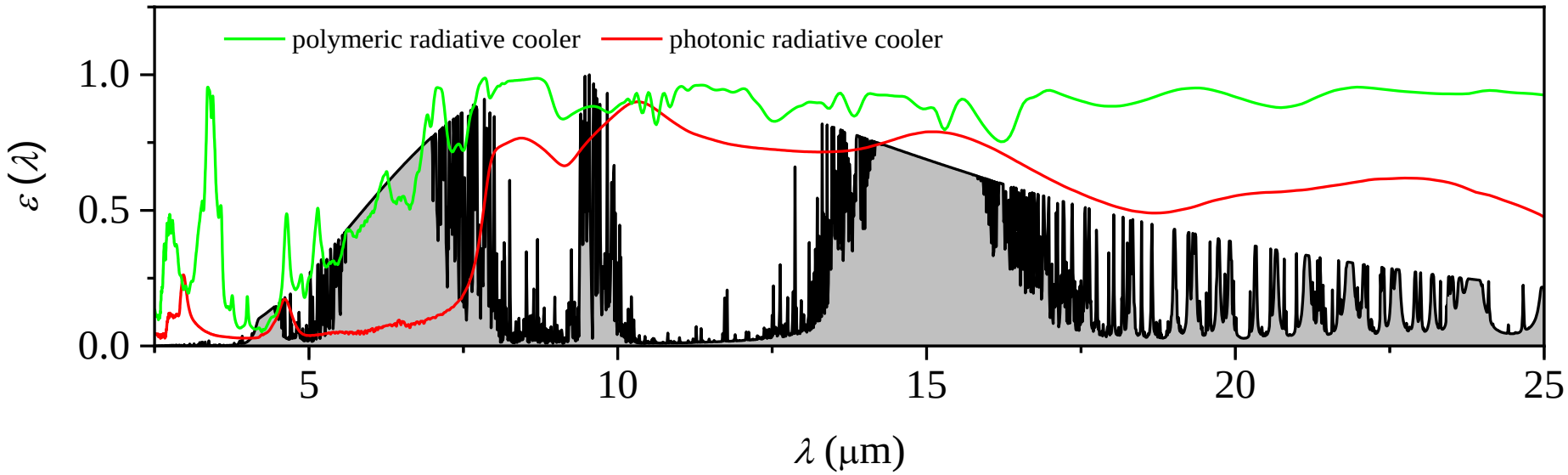

(b)

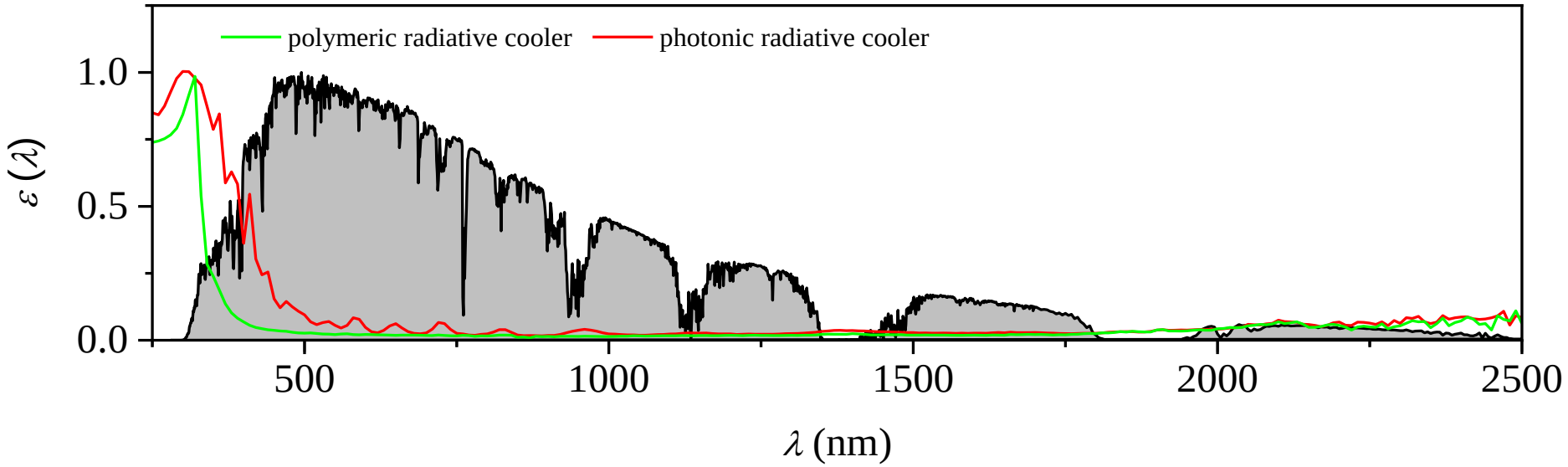
polymeric radiative cooler
photonic radiative cooler
1.0
0.5
0.0
ε (λ)
500
1000
1500
2000
2500
λ (nm)

Figure 2. (a) A schematic diagram; and (b) a picture of experimental setup for outdoor field investigations.

(a)

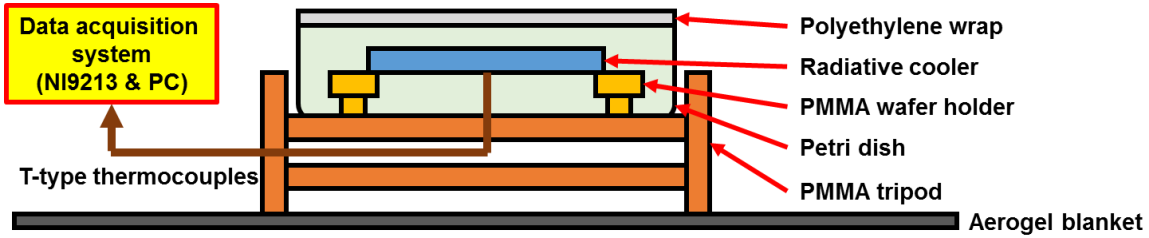

(b)

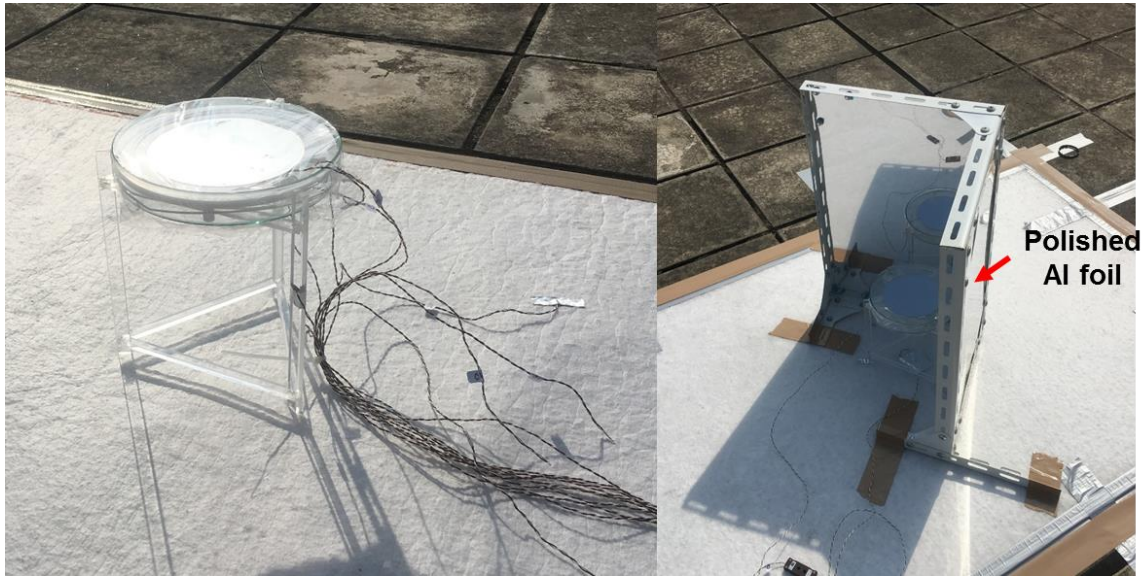

Figure 3. Temporary profiles of measured ambient temperature T_{amb} at site and surface temperatures $T_{w,0}$ of all examined devices, and recorded hourly ambient temperature T_{amb}, relative humidity ϕ, cloud fraction f_c and solar intensity I_{sun} from neighboring weather stations operated by The Hong Kong Observatory on (a) a dry and cloudless day; and (b) a humid and cloudy day.

(a)

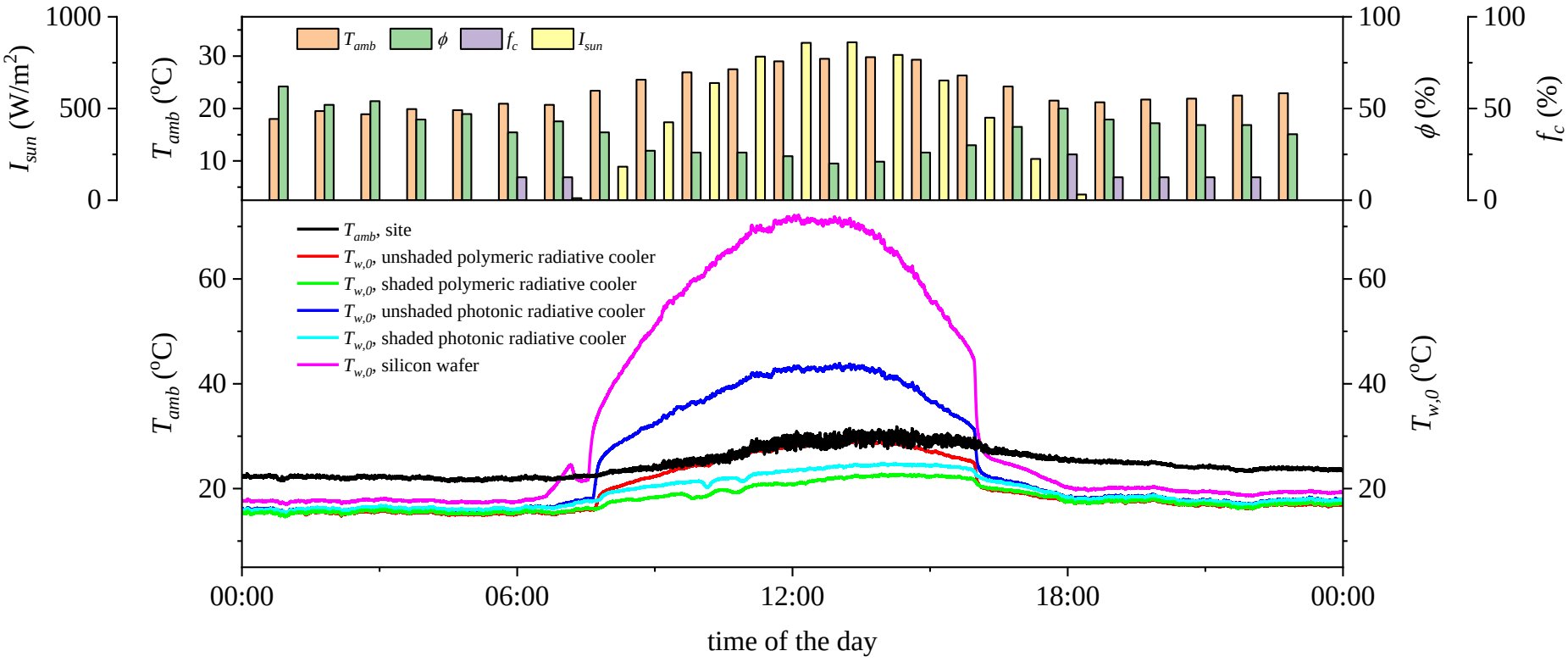

(b)

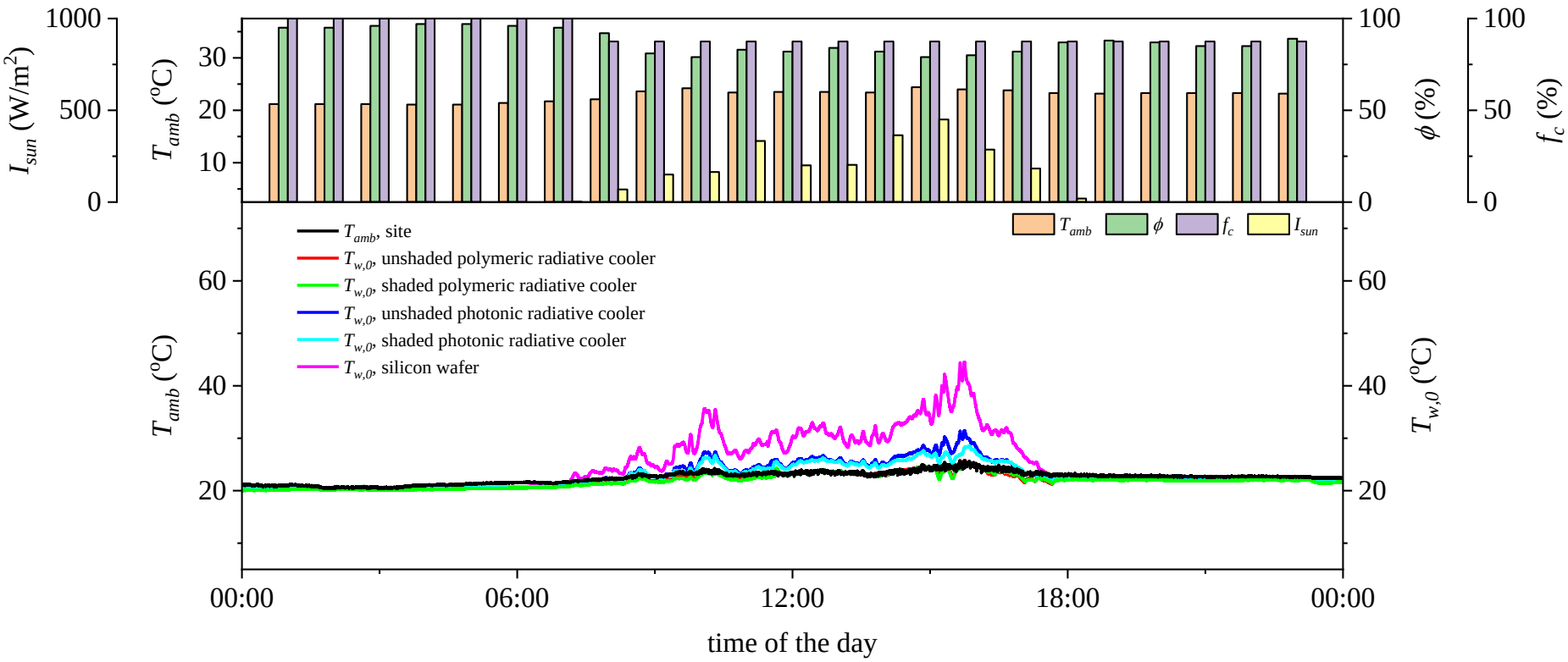
1000
500
0
I_{sun} (W/m^2)
30
20
10
T_{amb} (°C)
100
50
0
ϕ (%)
100
50
0
f_c (%)
T_{amb}
ϕ
f_c
I_{sun}
T_{amb}, site
$T_{w,0}$, unshaded polymeric radiative cooler
$T_{w,0}$, shaded polymeric radiative cooler
$T_{w,0}$, unshaded photonic radiative cooler
$T_{w,0}$, shaded photonic radiative cooler
$T_{w,0}$, silicon wafer
60
40
20
T_{amb} (°C)
60
40
20
$T_{w,0}$ (°C)
00:00
06:00
12:00
18:00
00:00
time of the day

Figure 4. The scatterplots of response variable of surface temperature reduction $\Delta T_{w,0}$ at nighttime against predictor variable of sky temperature difference ΔT_{sky} upon time-averaging, as well as the bivariate linear regression lines, for (a) shaded polymeric radiative cooler; (b) unshaded polymeric radiative cooler; (c) shaded photonic radiative cooler; (d) unshaded photonic radiative cooler; and (e) silicon wafer.

(a)

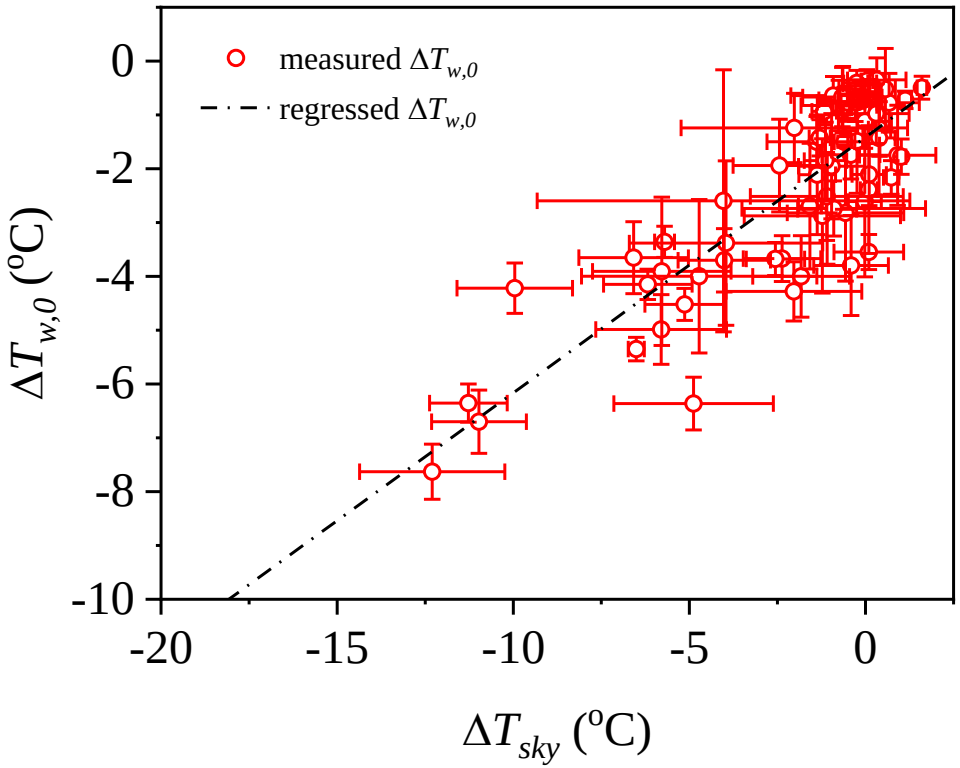

(b)

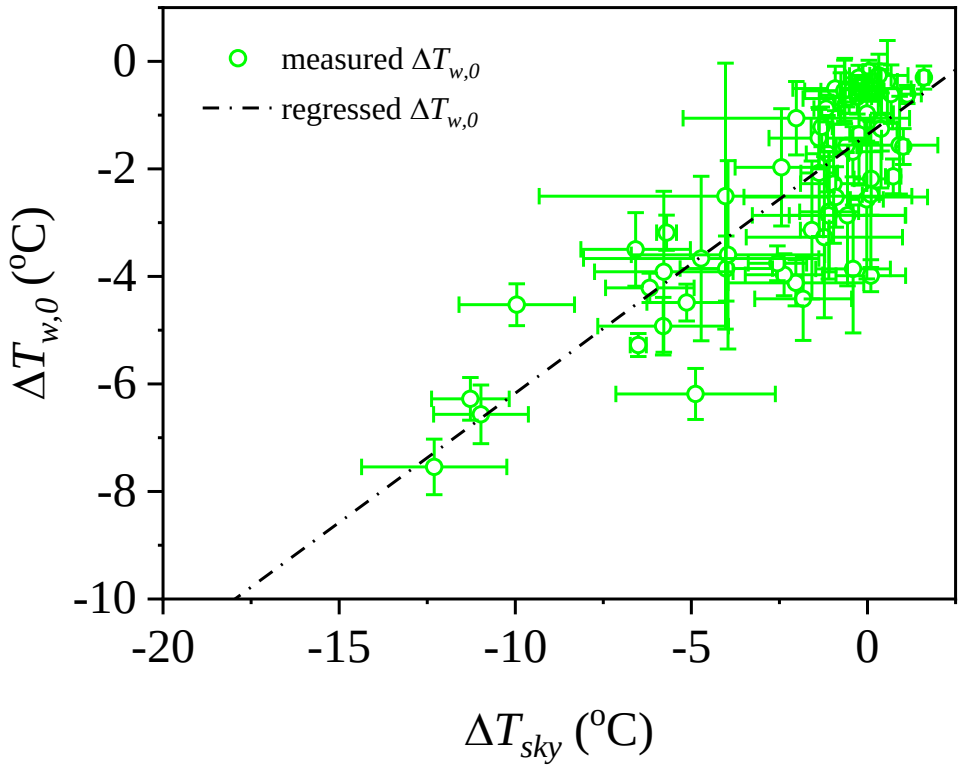
measured $\Delta T_{w,0}$
regressed $\Delta T_{w,0}$
0
-2
-4
-6
-8
-10
-20
-15
-10
-5
0
$\Delta T_{w,0}$ (°C)
ΔT_{sky} (°C)

(c)

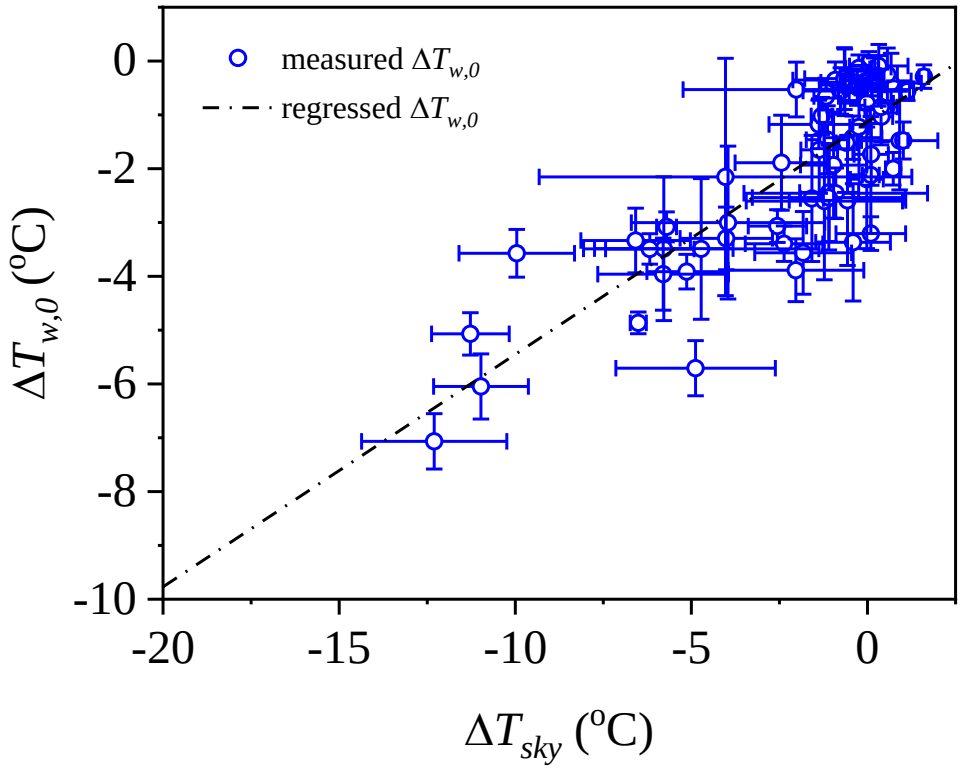
measured $\Delta T_{w,0}$
regressed $\Delta T_{w,0}$
0
-2
-4
-6
-8
-10
-20
-15
-10
-5
0
$\Delta T_{w,0}$ (°C)
ΔT_{sky} (°C)

(d)

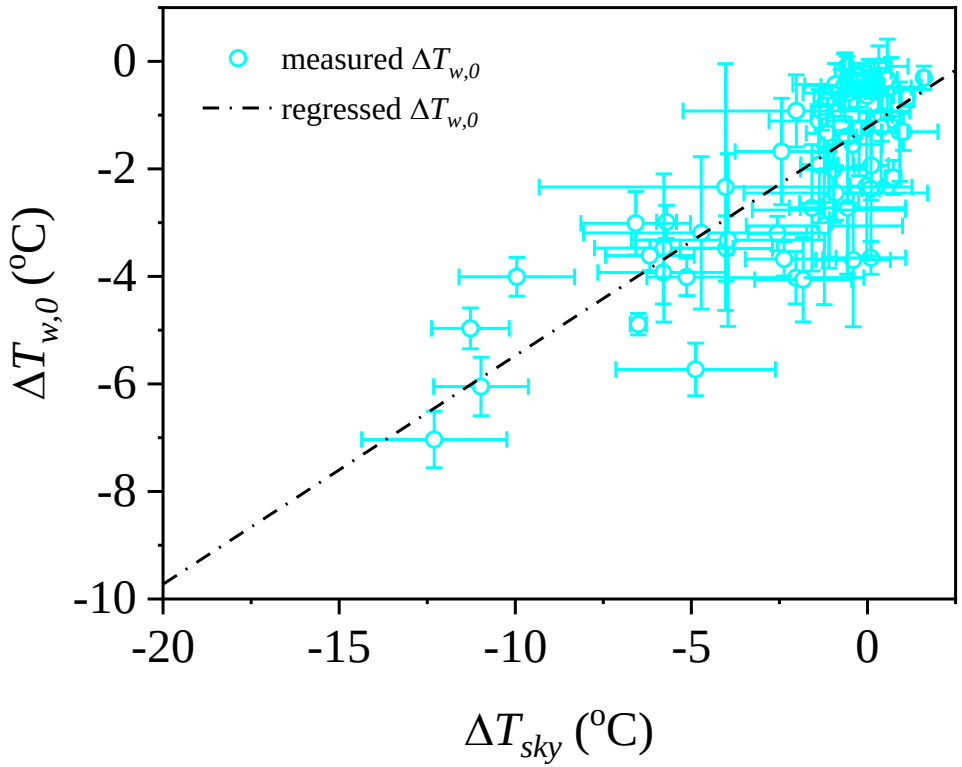
measured $\Delta T_{w,0}$
regressed $\Delta T_{w,0}$
0
-2
-4
-6
-8
-10
-20
-15
-10
-5
0
$\Delta T_{w,0}$ (°C)
ΔT_{sky} (°C)

(e)

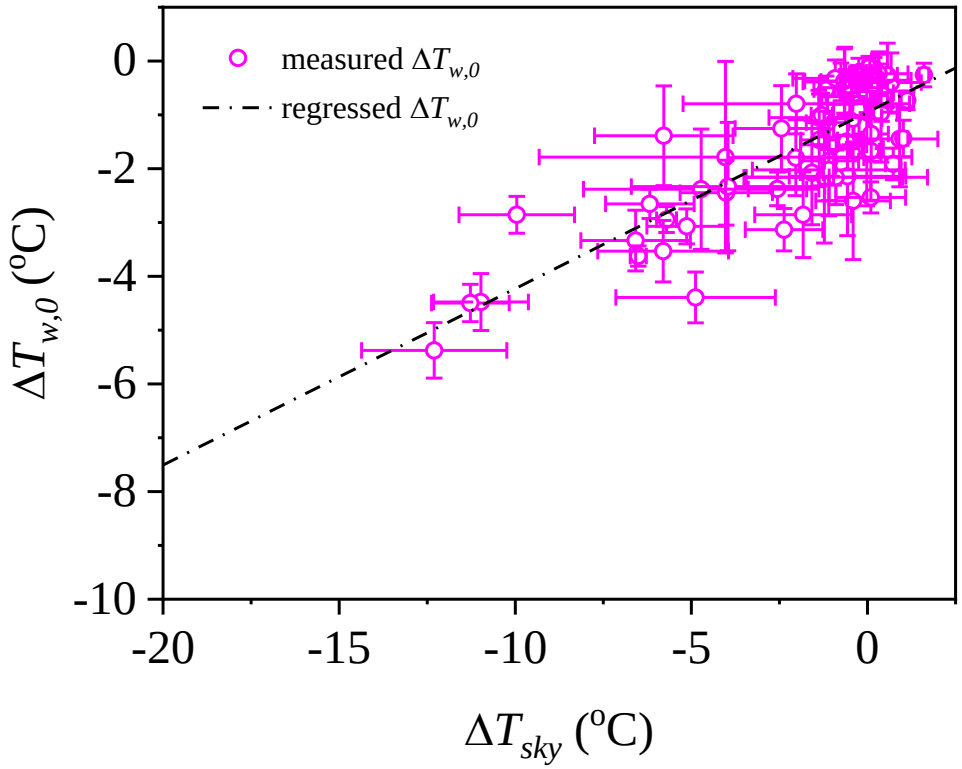
measured $\Delta T_{w,0}$
regressed $\Delta T_{w,0}$
0
-2
-4
-6
-8
-10
-20
-15
-10
-5
0
$\Delta T_{w,0}$ (°C)
ΔT_{sky} (°C)

Figure 5. The scatterplots of response variable of surface temperature reduction $\Delta T_{w,0}$ at daytime against predictor variable of sky temperature difference ΔT_{sky} upon time-averaging, as well as the bivariate and multivariate regression lines, for (a) shaded polymeric radiative cooler; (b) unshaded polymeric radiative cooler; (c) shaded photonic radiative cooler; (d) unshaded photonic radiative cooler; and (e) silicon wafer.

(a)

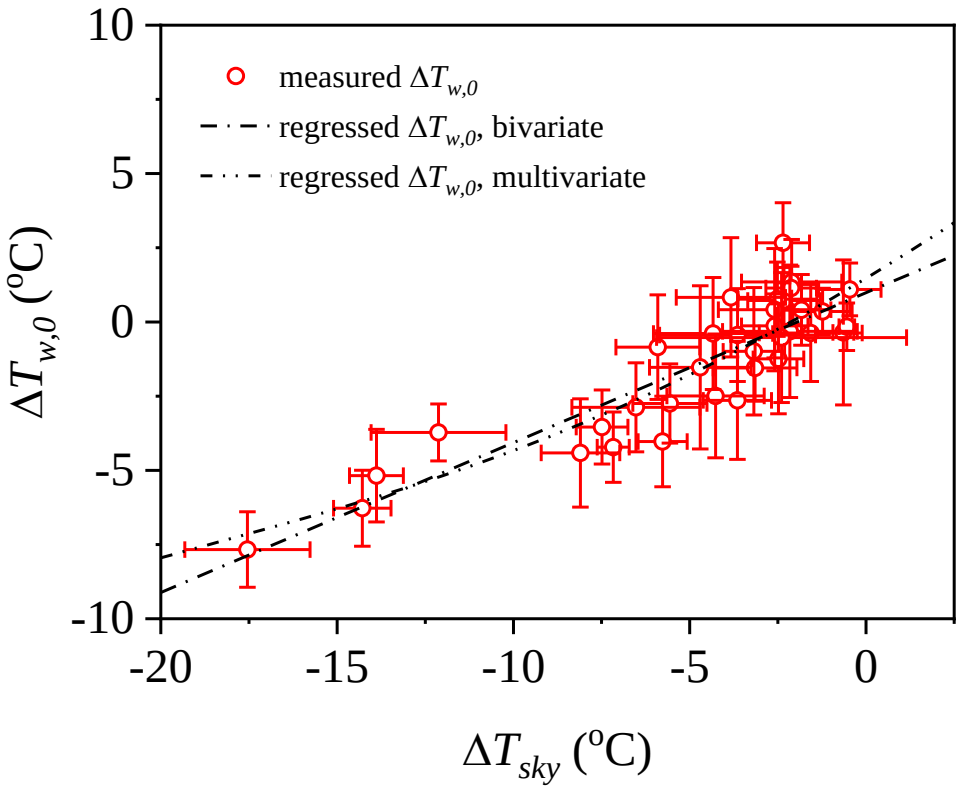

(b)

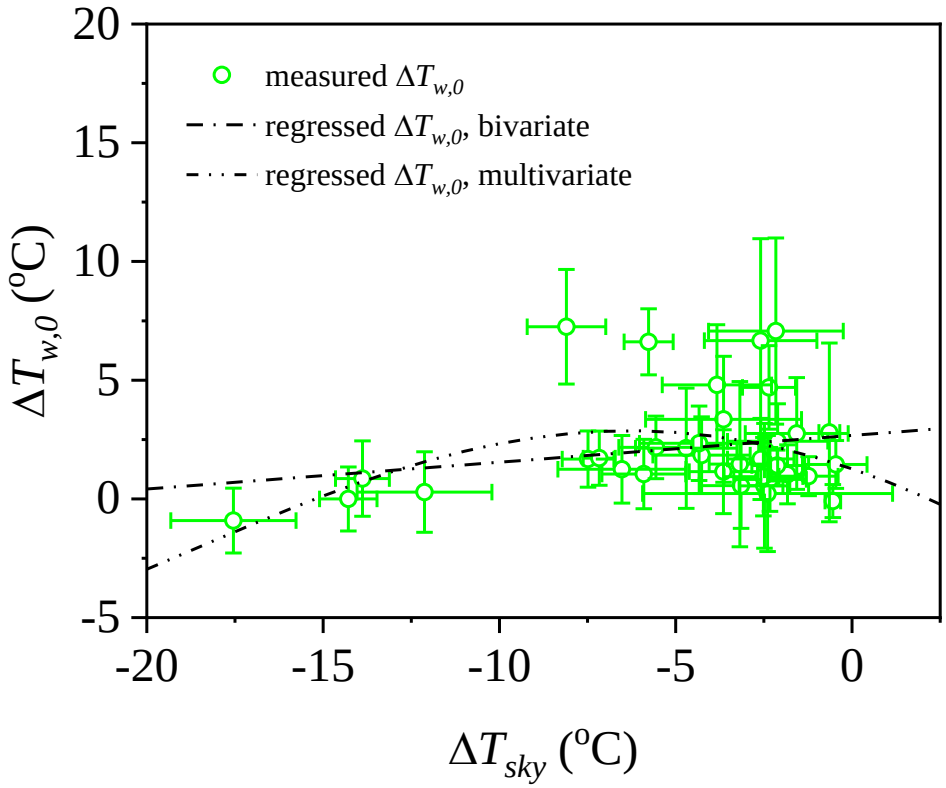
measured $\Delta T_{w,0}$
regressed $\Delta T_{w,0}$, bivariate
regressed $\Delta T_{w,0}$, multivariate
$\Delta T_{w,0}$ (°C)
ΔT_{sky} (°C)
20
15
10
5
0
-5
-20
-15
-10
-5
0

(c)

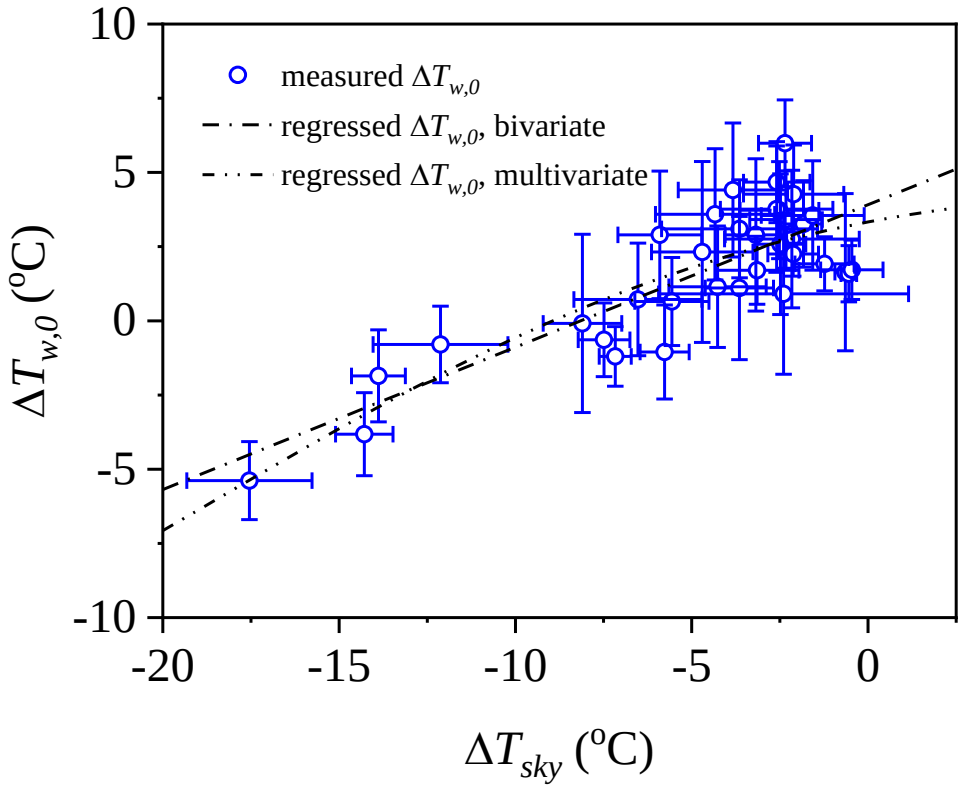
10
5
0
-5
-10
-20
-15
-10
-5
0
measured $\Delta T_{w,0}$
regressed $\Delta T_{w,0}$, bivariate
regressed $\Delta T_{w,0}$, multivariate
$\Delta T_{w,0}$ (°C)
ΔT_{sky} (°C)

(d)

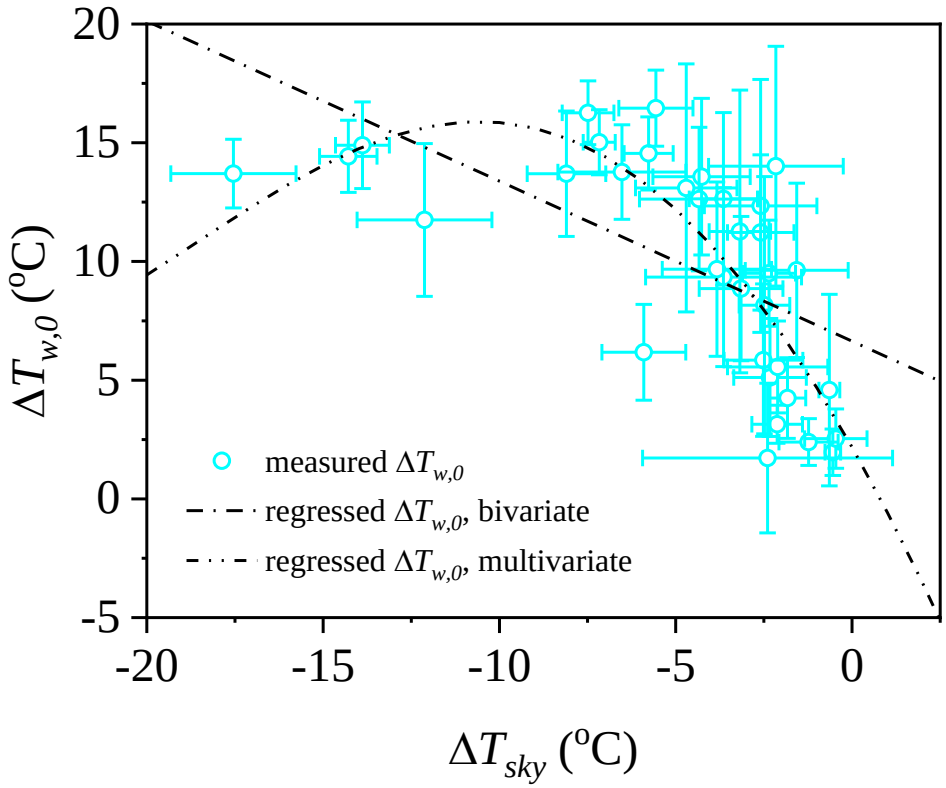
20
15
10
5
0
-5
-20
-15
-10
-5
0
$\Delta T_{w,0}$ (°C)
ΔT_{sky} (°C)
measured $\Delta T_{w,0}$
regressed $\Delta T_{w,0}$, bivariate
regressed $\Delta T_{w,0}$, multivariate

(e)

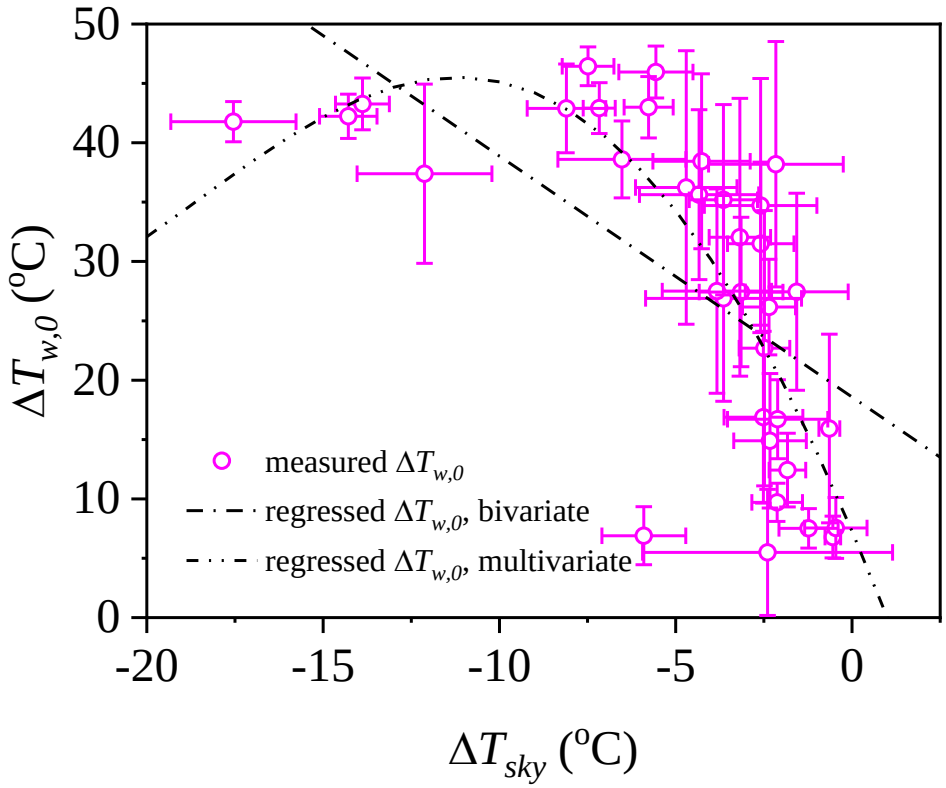
50
40
30
20
10
0
-20
-15
-10
-5
0
$\Delta T_{w,0}$ (°C)
ΔT_{sky} (°C)
measured $\Delta T_{w,0}$
regressed $\Delta T_{w,0}$, bivariate
regressed $\Delta T_{w,0}$, multivariate

Figure 6. Local historical meteorological data pairs of the (a) peak solar intensity I_{sun} against sky temperature difference ΔT_{sky}; and (b) dimensionless peak solar intensity I^*_{sun} against dimensionless sky temperature difference ΔT^*_{sky}; as well as the (c) frequency distribution of ΔT_{sky}, collected by the weather stations operated by The Hong Kong Observatory during the period of 2015 – 2017.

(a)

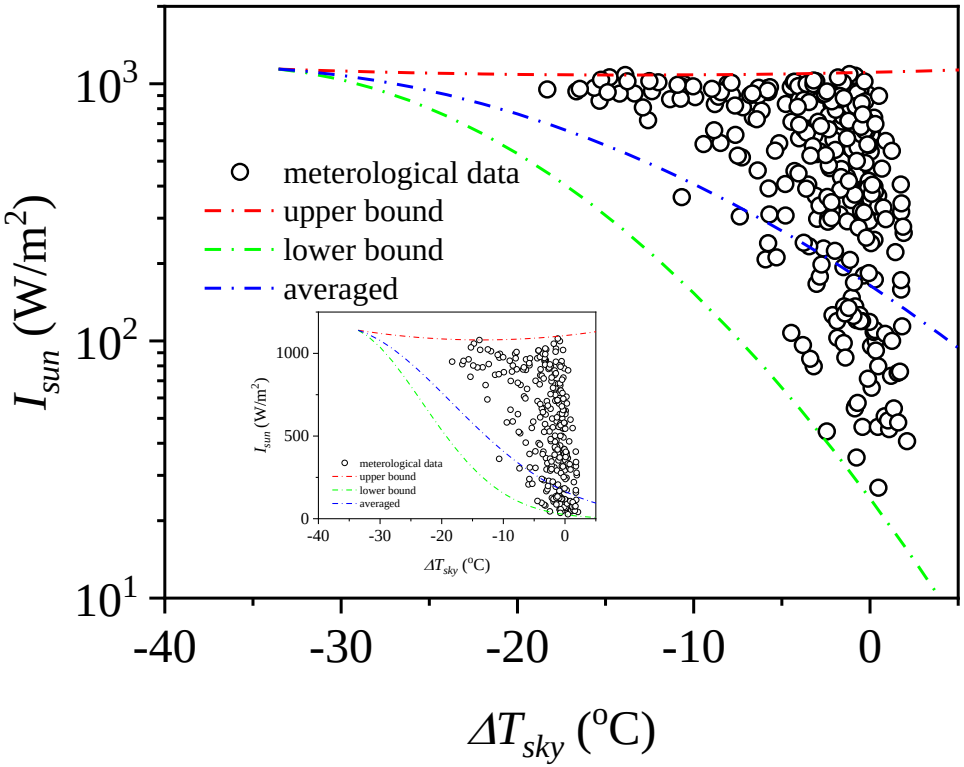

(b)

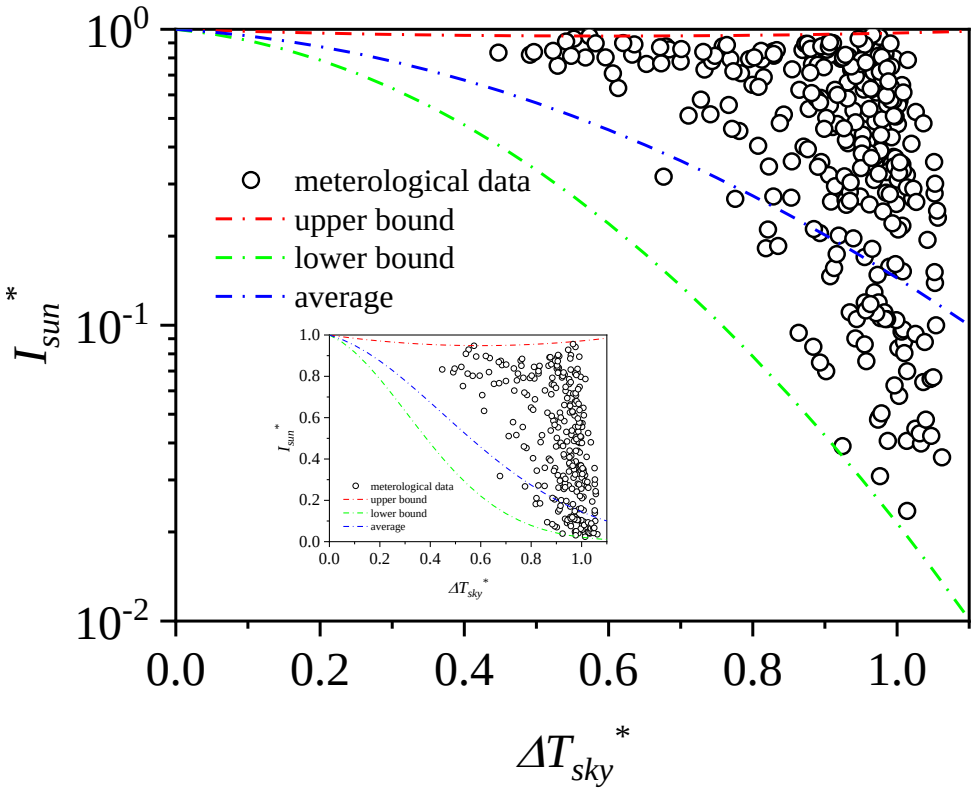
meterological data
upper bound
lower bound
average
I_{sun}^*
ΔT_{sky}^*
10^0
10^{-1}
10^{-2}
0.0
0.2
0.4
0.6
0.8
1.0

(c)

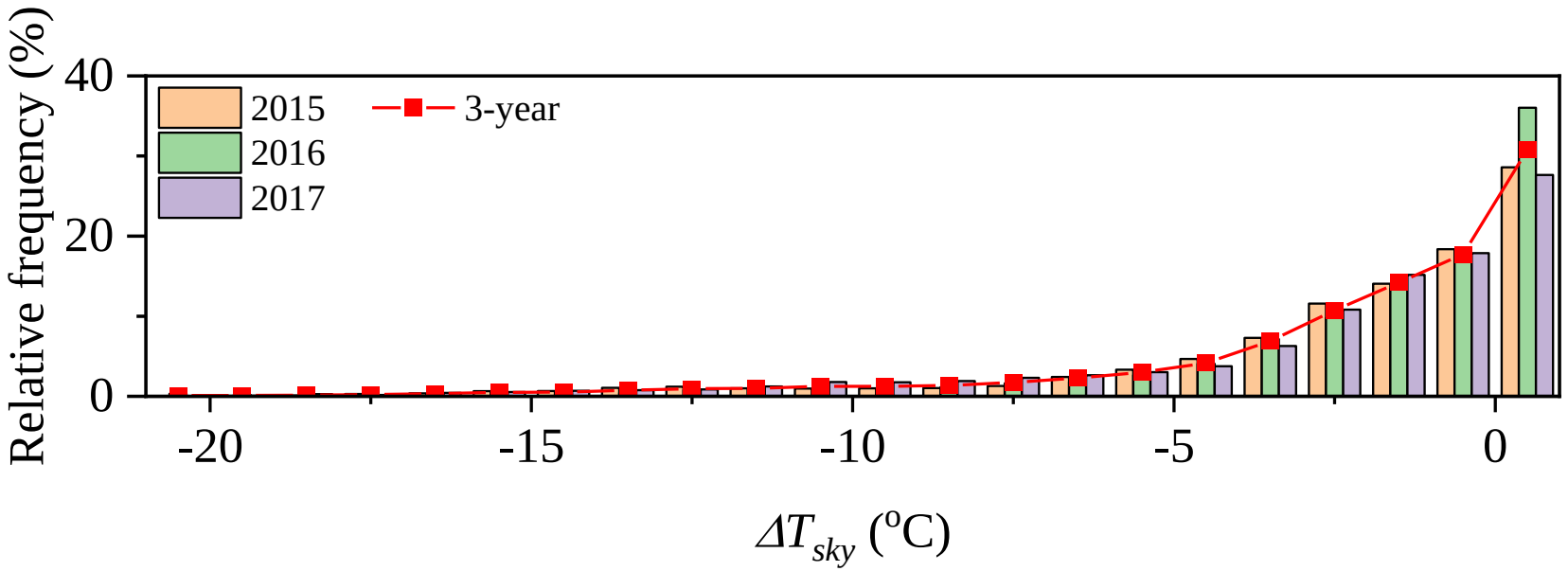
Relative frequency (%)
40
20
0
2015
2016
2017
3-year
-20
-15
-10
-5
0
ΔT_{sky} (°C)

References

[1] Raman, A. P., Anoma, M. A., Zhu, L., Rephaeli, E., Fan, S. (2014). Passive radiative cooling below ambient air temperature under direct sunlight. *Nature*, **515**, 540 – 544.

[2] Chen, Z., Zhu, L., Raman, A., Fan, S. (2016). Radiative cooling to deep sub-freezing temperatures through a 24-h day-night cycle. *Nature Communications*, **7**, 13729.

[3] Zou, J., Jurado, Z., Chen, Z., Fan, S., Minnich, A. J. (2017). Daytime radiative cooling using near-black infrared emitters. *ACS Photonics*, **4**, 626 – 630.

[4] Zhai, Y., Ma, Y., David, S. N., Zhao, D., Lou, R., Tan, G., Yang, R., Yin, X. (2017). Scalable manufactured randomized glass-polymer hybrid metamaterial for daytime radiative cooling. *Science*, **355**, 1062 – 1066.

[5] Hossain, M. M., Jia, B., Gu, M. (2015). A metamaterial emitter for highly efficient radiative cooling. *Advanced Optical Materials*, **3**, 1047 – 1051.

[6] Zou, C., Ren, G., Hossain, M. M., Nirantar, S., Withayachumnankul, W., Ahmed, T., Bhaskaran, M., Sriram, S., Gu, M., Fumeaux, C. (2017). Metal-loaded dielectric resonator metasurfaces for radiative cooling. *Advanced Optical Materials*, **5**, 1700460.

[7] Yu, N., Mandal, J., Overvig, A., Shi, N. N. (2016). Systems and methods for radiative cooling and heating. US patent no: WO2016205717A1.

[8] Goldstein, E. A., Raman, A. P., Fan, S. (2017). Sub-ambient non-evaporative fluid cooling with the sky. *Nature Energy*, **2**, 17143.

[9] Zhao, D., Aili, A., Zhai, Y., Lu, J., Kidd, D., Tan, G., Yin, X., Yang, R. (2019). Subambient cooling of water: Toward real-world applications of daytime radiative cooling. *Joule*, **3**, 111 – 123.

[10] Wang, W., Fernandez, N., Katipamula, S., Alvine, K. (2018). Performance assessment of a photonic radiative cooling system for office buildings, *Renewable Energy*, **118**, 265-277.

[11] Zhao, B., Pei, G., Raman, A. P. (2020). Modeling and optimization of radiative cooling based thermoelectric generators. *Applied Physics Letters*, **117**, 163903.

[12] Ishii, S., Dao, T. D., Nagao, T. (2020). Radiative cooling for continuous thermoelectric power generation in day and night. *Applied Physics Letter*, **117**, 013901.

[13] Zhao, D., Yin, X., Xu, J., Tan, G., Yang, R. (2020). Radiative sky cooling-assisted thermoelectric cooling system for building applications. *Energy*, **190**, 116322.

[14] Bao, H., Yan, C., Wang, B., Fang, X., Zhao, C. Y., Ruan, X. (2017). Double-layer nanoparticle-based coatings for efficient terrestrial radiative cooling. *Solar Energy Materials and Solar Cells*, **168**, 78 – 84.

[15] Tso, C. Y., Chan, K. C., Chao, C. Y. H. (2017). A field investigation of passive radiative cooling under Hong Kong's climate. *Renewable Energy*, **106**, 52 – 61.

[16] Jeong, S. Y., Tso, C. Y., Ha, J. Y., Wong, Y. M., Chao, C. Y. H., Huang, B., Qiu, H. (2019). Field investigation of a photonic multi-layered TiO_2 passive radiative cooler in sub-tropical climate. *Renewable Energy*, **146**, 44 – 55.

[17] Jeong, S. Y., Tso, C. Y., Wong, Y. M., Chao, C. Y. H., Huang, B. (2019). Daytime passive radiative cooling by ultra emissive bio-inspired polymeric surface. *Solar Energy Materials and Solar Cells*, **206**, 110296.

[18] Han, D., Ng, B. F., Wan, M. P. (2020). Preliminary study of passive radiative cooling under Singapore's tropical climate. *Solar Energy Materials and Solar Cells*, **206**, 110270.

[19] Han, D., Fei, J., Li, H., Ng, B. F. (2022). The criteria to achieving sub-ambient radiative cooling and its limits in tropical daytime. *Building and Environment*, **221**, 109281.

[20] Huang, J., Lin, C., Li, Y., Huang, B. (2022). Effect of humidity, aerosol, and cloud on subambient radiative cooling. *International Journal of Heat and Mass Transfer*, **186**, 122438.

[21] Li, M., Peterson, H. B., Coimbra, C. F. M. (2019). Radiative cooling resource maps for the contiguous United States. *Journal of Renewable and Sustainable Energy*, **11**, 036501.

[22] Zhu, Y., Qian, H., Yang, R., Zhao, D. (2021). Radiative sky cooling potential maps of China based on atmospheric spectral emissivity. *Solar Energy*, **218**, 195 – 210.

[23] Chen, J., Lu, L., Gong, Q. (2021). A new study on passive radiative sky cooling resource maps of China. *Energy Conversion and Management*, **237**, 114132.

[24] Berk, A., Conforti, P., Kennett, R., Perkins, T., Hawes, F., van den Bosch, J. (2014). MODTRAN 6: A major upgrade of the MODTRAN radiative transfer code. *2014 6th Workshop on Hyperspectral Image and Signal Processing: Evolution in Remote Sensing*, 1 – 4.

[25] Berk, A., Acharya, P. K., Bernstein, L. S., Anderson, G. P., Lewis, P., Chetwynd, J. H., Hoke, M. L. (2008). Band model method for modeling atmospheric propagation at arbitrarily fine spectral resolution. US patent no: 7433806.

[26] Alduchov, O. A., Eskrige, R. E. (1996). Improved Magnus form approximation of saturation vapor pressure. *Journal of Applied Meteorology*, **35**, 601 – 609.

[27] Brunt, D. (1932). Notes on radiation in the atmosphere I. *Quarterly Journal of the Royal Meteorological Society*, **58**, 389 – 420.

[28] Swinbank, W. C. (1963). Long-wave radiation from clear skies. *Quarterly Journal of the Royal Meteorological Society*, **89**, 339 – 348.

[29] Idso, S. B., Jackson, R. D. (1969). Thermal radiation from the atmosphere. *Journal of Geophysical Research*, **74**, 5397 – 5403.

[30] Staley, D. O., Jurica, G. M. (1972). Effective atmospheric emissivity under clear skies. *Journal of Applied Meteorology*, **11**, 349 – 356.

[31] Brutsaert, W. (1975). On a derivable formula for long-wave radiation from clear skies. *Water Resources Research*, **11**, 742 – 744.

[32] Satterlund, D. R. (1979). An improved equation for estimating long-wave radiation from the atmosphere. *Water Resources Research*, **15**, 1649 – 1650.

[33] Idso, S. B. (1981). A set of equations for full spectrum and 8- to 14-μm and 10.5- to 12.5-μm thermal radiation from cloudless skies. *Water Resources Research*, **17**, 295 – 304.

[34] Berdahl, P., Fromberg, R. (1982). The thermal radiance of clear skies. *Solar Energy*, **29**, 299 – 314.

[35] Berdahl, P., Martin, M. (1984). Emissivity of clear skies. *Solar Energy*, **32**, 663 – 664.

[36] Prata, A. J. (1996). A new long-wave formula for estimating downward clear-sky radiation at the surface. *Quarterly Journal of the Royal Meteorological Society*, **122**, 1127 – 1151.

[37] Dilley, A. C., O'brien, D. M. (1998). Estimating downward clear sky long-wave irradiance at the surface from screen temperature and precipitable water. *Quarterly Journal of the Royal Meteorological Society*, **124**, 1391 – 1401.

[38] Niemela, S., Raisanen, P., Savijarvi, H. (2001). Comparison of surface radiative flux parameterizations: Part I: Longwave radiation. *Atmospheric Research*, **58**, 1 – 18.

[39] Iziomon, M. G., Mayer, H., Matzarakis, A. (2003). Downward atmospheric longwave irradiance under clear and cloudy skies: measurement and parameterization. *Journal of Atmospheric and Solar-terrestrial Physics*, **65**, 1107 – 1116.

[40] Ruckstuhl, C., Philipona, R., Morland, J., Ohmura, A. (2007). Observed relationship between surface specific humidity, integrated water vapor, and longwave downward radiation at different altitudes. *Journal of Geophysical Research: Atmospheres*, **112**, D03302.

[41] Dai, Q., Fang, X. (2014). A new model for atmospheric radiation under clear sky condition at various altitudes. *Advances in Space Research*, **54**, 1044 – 1048.

[42] Carmona, F., Rivas, R., Caselles, V. (2014). Estimation of daytime downward longwave radiation under clear and cloudy skies conditions over a sub-humid region. *Theoretical and Applied Climatology*, **115**, 281 – 295.

[43] Culf, A. D., Gash, J. H. C. (1993). Longwave radiation from clear skies in Niger: A comparison of observations with simple formulas. *Journal of Applied Meteorology*, **32**, 539 – 547.

[44] Perez-Garcia, M. (2004). Simplified modeling of the nocturnal clear sky atmospheric radiation for environmental applications. *Ecological Modeling*, 180, 395 – 406.

[45] Lhomme, J. P., Vacher, J. J., Rocheteau, A. (2007). Estimating downward long-wave radiation on the Andean Altiplano. *Agricultural and Forest Meteorology*, **145**, 139 – 148.

[46] Bilbao, J., De Miguel, A. H. (2007). Estimation of daylight downward longwave atmospheric irradiance under clear-sky and all-sky conditions. *Journal of Applied Meteorology and Climatology*, **46**, 878 – 889.

[47] Choi, M., Jacobs, J. M., Kustas, W. P. (2008). Assessment of clear and cloudy sky parameterizations for daily downwelling longwave radiation over different land surfaces in Florida, USA. *Geophysical Research Letters*, **35**, L20402.

[48] Alados, I., Foyo-Moreno, I., Alados-Arboledas, L. (2012). Estimation of downwelling longwave irradiance under all-sky conditions. *International Journal of Climatology*, **32**, 781 – 793.

[49] Marthews, T. R., Malhi, Y., Iwata, H. (2011). Calculating downward longwave radiation under clear and cloudy conditions over a tropical lowland forest site: an evaluation of model schemes for hourly data. *Theoretical and Applied Climatology*, **107**, 461 – 477.

[50] Li, M., Jiang, Y., Coimbra, C. F. M. (2017). On the determination of atmospheric longwave irradiance under all-sky conditions. *Solar Energy*, **144**, 40 – 48.

[51] Alados-Arboledas, L., Vida, J., Olmo, F. J. (1995). The estimation of thermal atmospheric radiation under cloudy conditions. *International Journal of Climatology*, **15**, 107 – 116.

[52] Crawford, T. M., Duchon, C. E. (1999). An improved parametrization for estimating effective atmospheric emissivity for use in calculating daytime downwelling longwave radiations, *Journal of Applied Meteorology*, **38**, 474 – 480.

[53] Sugita, M., Brutsaert, W. (1993). Cloud effect in the estimation of instantaneous downward long-wave radiation. *Water Resources Research*, **29**, 599 – 605.

[54] Maykut, G. A., Church, P. F. (1973). Radiation climate of Barrow, Alaska, 1962 – 66. *Journal of Applied Meteorology*, **12**, 620 – 628.

[55] Konzelmann, T., van der Wal, R. S. W., Greuell, W., Bintanja, R., Henneken, E. A., Abe-Ouchi, A. (1994). Parametrization of global and longwave incoming radiation for the Greenland Ice Sheet. *Global and Planetary Change*, **9**, 143 – 164.

[56] Duarte, H. F., Dias, N. L., Maggiotto, S. R. (2006). Assessing daytime downward longwave radiation estimates for clear and cloudy skies in Southern Brazil. *Agricultural and Forest Meteorology*, **139**, 171 – 181.

[57] Infrared atmospheric transmission spectrum at Mauna Kea (accessed April, 2017), http://www.gemini.edu/sciops/telescopes-and-sites/observingcondition-constraints/ir-transmission-spectra.

[58] Liou, K. N. (2002). *An Introduction to Atmospheric Radiation (2nd edition)*, Elsevier, United States of America.

[59] Wallace, J. M., Hobbs, P. V. (2006). *Atmospheric Science. An Introductory Survey (2nd edition)*, Elsevier, Canada.

[60] Liou, K. N., Yang, P. (2016). *Light Scattering by Ice Crystals, Fundamentals and Applications*, Cambridge University Press, United Kingdom.

[61] Rayleigh, L. (1899). On the transmission of light through an atmosphere containing small particles in suspension, and on the origin of the blue of the sky. *The London, Edinburgh, and Dublin Philosophical Magazine and Journal of Science*, 47, 375 – 384.

[62] Meinel, A. B., Meinel, M. P. (1976). *Applied Solar Energy. An Introduction*, Addison-Wesley, United States of America.

[63] Winkelmann, F., Birdsall, B., Buhl, W., Ellington, K. L., Erdem, A. E., Hirsch, J. J., Gates, S. D. (1993). *DOE-2 supplement: version 2.1 e*. Lawrence Berkeley Laboratory, United States of America.

[64] Crawley, D. B., Lawrie, L. K., Winkelmann, F. C., Buhl, W. F., Huang, Y. J., Pedersen, C. O., Strand, R. K., Liesen, R. J., Fisher, D. E., Witte, M. J., Glazer, J. (2001). EnergyPlus: creating a new-generation building energy simulation program. *Energy and Buildings*, **33**, 319 – 331.

[65] Kalogirou, S. A., Bojic, M. (2000). Artificial neural networks for the prediction of the energy consumption of a passive solar building. *Energy*, **25**, 479 – 491.

[66] Kalogirou, S. A. (2006). Artificial neural networks in energy applications in buildings. *International Journal of Low-Carbon Technologies*, **1**, 201 – 216.

[67] Wong, R. Y. M., Tso, C. Y., Chao, C. Y. H. (2021). Thermo-radiative energy conversion efficiency of a passive radiative fluid cooling system. *Renewable Energy*, **180**, 700 – 711.

[68] Goldstein, E. A., Raman, A. P., Fan, S. (2017). Sub-ambient non-evaporative fluid cooling with the sky. *Nature Energy*, **2**, 17143.

[69] Zhao, D., Aili, A., Zhai, Y., Lu, J., Kidd, D., Tan, G., Yin, X., Yang, R. (2019). Subambient cooling of water: Toward real-world applications of daytime radiative cooling. *Joule*, **3**, 111 – 123.

[70] Aili, A., Zhao, D., Lu, J., Zhai, Y., Yin, X., Tan, G., Yang, R. (2019). A kw-scale, 24-hour continuously operational, radiative sky cooling system: Experimental demonstration and predictive modelling. *Energy Conversion and Management*, **186**, 586 – 596.

[71] Electrical and Mechanical Services Department - Hong Kong Energy End Use Data 2022 (accessed July 2022), https://www.emsd.gov.hk/filemanager/en/content_762/HKEEUD2022.pdf

[72] Environmental Protection Department – Guidelines to Account for and Report on Greenhouse Gas Emissions and Removals for Buildings (Commercial, Residential or Institutional Purposes) in Hong Kong (2010 Edition) (accessed July 2022), https://www.climateready.gov.hk/files/pdf/Guidelines_English_2010.pdf

Declaration of interests

☒ The authors declare that they have no known competing financial interests or personal relationships that could have appeared to influence the work reported in this paper.

☐The authors declare the following financial interests/personal relationships which may be considered as potential competing interests:

Author Roles

Ross Y. M. Wong: Conceptualization, Methodology, Software, Validation, Formal Analysis, Investigation, Writing-Original Draft, Visualization. **C. Y. Tso**: Supervision, Project administration, Funding acquisition, Resources, Conceptualization, Writing-Review and Editing. **S. Y. Jeong**: Validation, Investigation, Writing – Review and Editing. **S. C. Fu**: Supervision, Conceptualization, Writing-Review and Editing. **Christopher Y. H. Chao**: Supervision, Project administration, Funding acquisition, Resources, Writing – Review and Editing.

Term	**Definition**
Conceptualization	Ideas; formulation or evolution of overarching research goals and aims
Methodology	Development or design of methodology; creation of models
Software	Programming, software development; designing computer programs; implementation of the computer code and supporting algorithms; testing of existing code components
Validation	Verification, whether as a part of the activity or separate, of the overall replication/ reproducibility of results/experiments and other research outputs
Formal analysis	Application of statistical, mathematical, computational, or other formal techniques to analyze or synthesize study data
Investigation	Conducting a research and investigation process, specifically performing the experiments, or data/evidence collection
Resources	Provision of study materials, reagents, materials, patients, laboratory samples, animals, instrumentation, computing resources, or other analysis tools
Data Curation	Management activities to annotate (produce metadata), scrub data and maintain research data (including software code, where it is necessary for interpreting the data itself) for initial use and later reuse

Writing - Original Draft	Preparation, creation and/or presentation of the published work, specifically writing the initial draft (including substantive translation)
Writing - Review & Editing	Preparation, creation and/or presentation of the published work by those from the original research group, specifically critical review, commentary or revision – including pre-or postpublication stages
Visualization	Preparation, creation and/or presentation of the published work, specifically visualization/ data presentation
Supervision	Oversight and leadership responsibility for the research activity planning and execution, including mentorship external to the core team
Project administration	Management and coordination responsibility for the research activity planning and execution
Funding acquisition	Acquisition of the financial support for the project leading to this publication